NSMB-A41484A

The structure and oxidation of the eye lens chaperone αA-crystallin

Authors:

Christoph J. O. Kaiser[1†], Carsten Peters[1†], Philipp W. N. Schmid[1], Maria Stavropoulou[1,2], Juan Zou[3], Vinay Dahiya[1], Evgeny V. Mymrikov[1,4], Beate Rockel[1], Sam Asami[1,2], Martin Haslbeck[1], Juri Rappsilber[3,5], Bernd Reif[1,2], Martin Zacharias[6], Johannes Buchner[1*] and Sevil Weinkauf[1*]

Affiliations:

[1] Center for Integrated Protein Science Munich at the Department Chemie, Technische Universität München, Lichtenbergstrasse 4, D-85747 Garching, Germany

[2] Institute of Structural Biology, Helmholtz Zentrum München, 85764, Neuherberg, Germany

[3] Wellcome Centre for Cell Biology, University of Edinburgh, Edinburgh EH9 3BF, United Kingdom

[4] current address: Institute for Biochemistry and Molecular Biology, Albert-Ludwigs-Universität Freiburg, Stefan-Meier-Straße 17, 79104 Freiburg, Germany

[5] Bioanalytics, Institute of Biotechnology, Technische Universität Berlin, Gustav-Meyer-Allee 25, 13355 Berlin, Germany

[6] Center for Integrated Protein Science Munich at the Physics Department, Technische Universität München, James-Franck-Strasse 1, D-85748 Garching, Germany

* **Correspondence to:** sevil.weinkauf@tum.de; johannes.buchner@tum.de

† These authors contributed equally to this work.

Keywords:

αA-crystallin / small heat shock protein / domain swapping / cryo-electron microscopy / disulfide bond

Abstract

The small heat shock protein (sHsp) αA-crystallin is an essential component of the vertebrate eye lens. It forms heterogeneous ensembles of oligomeric states and is important for the transparency and optical properties of the eye lens. We determined the structures of human αA-crystallin oligomers by a combination of cryo-electron microscopy (cryo-EM), cross-linking/mass spectrometry (CLMS), nuclear magnetic resonance (NMR) spectroscopy and molecular modeling. The different oligomers interconvert by the addition or subtraction of tetramers as basic building blocks leading to mainly 12-, 16- and 20-meric assemblies in which interactions between N-termini of neighboring protomers play a predominant role in oligomer formation. Cross-dimer domain-swapping of the C-terminal region is an important determinant of αA-crystallin heterogeneity. Human αA-crystallin contains two cysteines which can form an intramolecular disulfide bond *in vivo*. We show that disulfide formation requires local conformational changes concomitant with oligomer dissociation. Oxidation leads to oligomers that are larger and destabilized against unfolding in comparison to the oligomers of reduced αA-crystallin. Yet they are chaperone active and can transfer the intramolecular disulfide to destabilized substrate proteins. Our results reveal novel aspects of the structure and function of αA-crystallin and provide a basis for further understanding of its role in the eye lens.

Introduction

The small heat shock proteins (sHsps) αA- and αB-crystallin are major constituents of the vertebrate eye lens[1]. They ensure lens transparency[1,2] and prevent lens proteins from aggregation[3,4]. Mutations in both α-crystallins result in cataract and in a variety of eye disorders, emphasizing their importance for the lens[2,5]. Besides the commonality of the processes in which αA- and αB-crystallin are involved, differences in their expression patterns and distribution in the lens exist[6-9]. Specifically, αA-crystallin is predominantly expressed in the eye lens. *In vitro* studies point towards mechanistic differences between αA- and αB-crystallin in suppressing the aggregation of model substrates[10,11] and mutations of conserved residues have different impact on the two crystallins[12].

Human αA-crystallin, a 19.9 kDa protein with 173 residues, consists of three structurally distinct regions: the conserved α-crystallin domain (ACD, residues 61-145) flanked by the N-terminal region (NTR, residues1-60) and the short, flexible C-terminal region (CTR, residues146-173)[13,14]. The ACD adopts a β-sandwich fold composed of two anti-parallel sheets of three and four β-strands, respectively. It dimerizes through the interaction of the β6+7-strands of two adjacent protomers ("β7-interface dimer")[15,16]. αA-crystallin assembles into polydisperse oligomers with extensive size heterogeneity and a constant exchange of subunits between oligomers[17-19]. There is yet no structural information available either for full-length αA-crystallin or for αA-crystallin in any oligomeric form. Consequently, the structural elements critical for assembly and those conferring plasticity to the oligomeric assembly are poorly understood. The involvement of the NTR in oligomer formation is indicated by the shift of the average oligomer ensemble to smaller species, dimers and/or tetramers, upon its truncation[20-23]. Studies on C-terminal truncation mutants of αA-crystallin from different organisms display significant disparities leaving the role of the CTR in oligomer formation still ill defined[18,21,24-27]. The CTR of αA-crystallin exhibits greater overall flexibility than that of αB-crystallin[28] including the segment containing the conserved IXI motif, which promotes oligomer formation by binding into the β4/β8 groove within the ACD of a neighboring protomer[29,30].

A characteristic of human αA-crystallin is the presence of two cysteines in its ACD, the invariant C131 found in most species and an additional cysteine at position 142 also found in αA-crystallin from primates and zebrafish (*Danio rerio*)[31]. C131 was predicted to be buried, whereas C142 was suggested to be fully solvent-exposed[32,33]. In the crystal structure of the zebrafish αA-crystallin ACD, the CTR covers C132 while leaving C143 accessible[16]. Notably, already in young human lenses and during the first ~30 years of age, ~45 % of αA-crystallin exhibit an intramolecular disulfide bond (henceforth denoted as oxidized αA-crystallin, αA_{ox}), in the remaining fraction the cysteines are in the free sulfhydryl form (reduced αA-crystallin, αA_{red})[34-37]. In young lenses, a subpopulation might form intermolecular disulfides as well[38]. With

ageing, the amount of αA_{ox} increases up to 90 %[36] and it becomes a major constituent of high molecular weight aggregates[39-41], concomitant with an age-dependent loss of the chaperone activity of α-crystallin[42]. αA_{red} is undetectable in cataractous lenses[35]. Despite their importance, the structural and functional consequences of αA-crystallin oxidation are yet unknown.

Here we present the architecture and plasticity of human αA-crystallin oligomers as well as the structural and functional consequences of its oxidation. The structures of human αA-crystallin assemblies and pseudo-atomic models of a 16-meric assembly reveal the domain-swapping of the CTR to be a key determinant of αA-crystallin heterogeneity. Formation of the intramolecular disulfide bond leads to distinct oligomers that are chaperone active and can transfer its intramolecular disulfide to destabilized substrate proteins.

Results

Oligomer architecture and conformational heterogeneity of reduced αA-crystallin

To determine the oligomer architecture of reduced human αA-crystallin, we employed single-particle cryo-EM (**Supplementary Fig. 1**). The initial analysis of ~74,000 projection images revealed two distinct populations, one containing round particles with 3-, 4- and 5-fold symmetries and diameters varying between 6 and 16 nm (**Supplementary Fig. 1b**), the other one comprising elongated structures with 2-fold symmetry and a nearly uniform long axis of 13-14 nm (**Supplementary Fig. 1c**). The two populations seemed to represent end- and side-on projections of a barrel-like architecture with varying subunit stoichiometries. On this basis, we established a 3D-reconstruction procedure which allowed us to assign ~ 80 % of the particles to 12-, 16- and 20-meric assemblies with abundances of approximately 36 %, 27 % and 19 % and calculate the corresponding 3D models (**Fig. 1**) at resolutions of 9.2 Å, 9.8 Å and 9.0 Å, respectively (**Supplementary Fig. 1h, Supplementary Table 1**).

According to the reconstructed EM volumes (**Fig. 1**), all three assemblies form hollow, barrel-like structures with a recurring unit resembling a tilted „Z“ comprising two substructures that are connected in the mid-plane of the barrel. Each of these substructures is large enough to accommodate an αA-crystallin dimer implying that the Z-shaped structures represent tetramers (dimers of dimers) which serve as building blocks of the oligomers. Notably, in the average structures of the 12- and 16-mers, adjacent tetramers are not connected in the equatorial plane of the barrel (**Fig. 1a,b)** whereas there is a well-resolved density bridging neighboring tetramers in the 20-mer (**Fig. 1c**).

To elucidate the structural variability of αA_{red} oligomers, each oligomer population was subjected to 3D sampling and classification which revealed that the density corresponding to an αA-crystallin dimer remains almost invariant within all three populations (**Supplementary Fig. 2**). In contrast, significant heterogeneity exists in areas where adjacent tetramers come together in apical and equatorial regions which most likely harbor the N- and/or C-termini. The oligomers differ in the density connecting the tetramers in the equatorial plane: this density is lacking in all sub-ensembles of the 12-mer population, while it is present in approximately 30 % of the 16-mer population and in all sub-ensembles of the 20-mer population (**Supplementary Fig. 2 and Supplementary Table 2**). The observed heterogeneity is suggestive of dynamic inter-subunit interactions involving N- and/or C-terminal regions. This conformational heterogeneity together with very similar projection views of different oligomers presumably limit the resolution of the reconstructions.

Pseudo-atomic model of the αA-crystallin 16-mer

To obtain pseudo-atomic models of the αA_{red} 16-mer, we subjected full-length protein to cross-linking and mass spectrometry. Using the cross-linker bis(sulfosuccinimidyl)suberate (BS3), we identified numerous intra- and intermolecular cross-links (**Supplementary Figs. 3,4 and Supplementary Table 3**). The data demonstrated the structural similarity of human αA-crystallin in its ACD and CTR to zebrafish and bovine αA-crystallin, as all distances between corresponding residue pairs resolved in the respective crystal structures were below 30 Å which is approximately the upper distance limit dictated by the utilized cross-linker[43] (**Supplementary Fig. 4f**).

The volume of the equatorial inter-tetramer density present in some 16-mer sub-populations is just large enough to accommodate the CTR (**Supplementary Fig. 2**). Together with its positioning, we reasoned that the variability within this area stems from 3D domain swapping of the CTR: in structural classes containing the equatorial inter-tetramer density, the IPV motif binds intermolecularly into the β4/β8 pocket of an adjacent protomer (3D domain-swapped configuration), while in classes lacking the density, it binds intramolecularly into the β4/β8 pocket of the same polypeptide chain (non-3D domain-swapped configuration). This view is supported by the occurrence of the CTRs in swapped and non-swapped configurations in bovine and zebrafish αA-crystallin ACD crystal structures, respectively[15,16]. Thus, we generated pseudo-atomic models of the αA_{red} 16-mer with the CTRs in both configurations using (i) shape and symmetry constraints from the cryo-EM envelopes differing in the equatorial inter-tetramer density, (ii) the crystal structures of truncated versions of bovine and zebrafish αA-crystallins as templates, and (iii) intra- and intermolecular distance restraints from cross-linking. During modeling using Molecular Dynamics Flexible Fitting (MDFF), a homology-modeled structure for the NTR (residues 1-60) was used which contained 3 short helices connected by flexible loops (**Supplementary Fig. 5a,b**). The structures of the central ACD (residues 61-145) and part of the CTR (residues 146-166) were derived from homology modeling based on the above-mentioned crystal structures. The residues 167-173 were not included into the model due to their flexibility[28]. The fitting procedure resulted in an ensemble of solutions with the NTRs of both apical (M_{ap}) and equatorial protomers (M_{eq}) adopting a variety of possible conformations (**Supplementary Fig. 5c,d**) consistent with their flexibility. Although no consensus structure could be derived for the NTR, its integration during the fitting process was crucial because it restricted the positioning of the central ACD and CTR. The best structures were selected based on RMSD, stereochemistry and cross correlation with respect to the cryo-EM density and further energy minimized.

In the final pseudo-atomic models of the αA_{red} 16-mer (**Fig. 2**) which fit best into the EM-map from all possible models and fulfill cross-linking restrains, all parts of the polypeptide chain are accommodated within the electron density. The models reveal that two protomers form a dimer

with a β7-interface. Interactions between N-termini mediate the association of two dimers across the equator to form a tetramer (equatorial N-terminal interface, eq-NI) (**Fig. 2a,d**), which is the recurring unit of the oligomer. Further N-terminal interactions between apical protomers of the tetramers (apical N-terminal interface, ap-NI) serve to form the 16-mer (**Fig. 2a**). The close proximity of the N-terminal segments is corroborated by intermolecular cross-links involving residues M1, K11, and T13 (**Supplementary Table 3**) which are all satisfied in our models. In contrast to the prevailing contribution of the NTR to oligomer formation, the CTR is barely involved in inter-subunit interactions. In both models (**Fig. 2a,b**), the CTRs of M_{ap} are in a non-3D domain-swapped configuration as the distance between apical protomers is too large compared to the length of the CTR to permit an intermolecular IXI-β4/β8 interaction. On the other hand, although the distance between M_{eq} of neighboring tetramers supports this interaction in both directionalities of the palindromic sequence, the CTR contributes to the assembly by 3D domain swapping in only ~30 % of the 16-mer population (**Fig. 2b,f**). 3D domain swapping creates an interface (equatorial C-terminal interface, eq-CI) in which the CTRs of M_{eq} from neighboring tetrameric units are in close proximity, consistent with the observed intermolecular cross-link K166-K166 (not used as a modeling constraint), and interact through electrostatic interactions involving residues downstream of the IXI motif (**Fig. 2b,f**).

3D domain-swapping of the C-terminal region in the αA-crystallin ensemble

12- and 20-meric αA_{red} assemblies share the modular architecture of the 16-mer (**Fig. 3a,b**). In all three cases, the tetramers have the same curvature. The ACD positions within the tetramers are identical. In 12- and 20-mers, the CTRs do also not swap domains in the apical regions due to the large distance between adjacent protomers. However, the CTRs of all M_{eq} are in the non-3D domain-swapped state in the 12-mer whereas those of the 20-mer connect neighboring tetramers by domain swapping (**Fig. 3**). As estimated from the relative abundances of all sub-populations, ~20 % of all CTRs are in the domain-swapped within the ensemble subset studied (**Supplementary Table 2**). Domain swapping of the CTR as suggested by cryo-EM would require large amplitude motions of the polypeptide chain also in the hinge region (I146-E156) adjacent to the ACD. The CTR of αA-crystallin displays significant flexibility and can be detected by solution-state NMR (residues G149-S173, **Fig. 3c**)[28]. To test the prevalence of 3D domain-swapping of the CTR in the reduced alphaA-crystallin ensemble, we we performed paramagnetic relaxation enhancement (PRE) experiments on αA_{red} labelled with the 3-(2-iodoacetamido)-proxyl spin label (IPSL) at the cysteine residues within the ACD (most likely C142). The spectra of the spin-labelled ^{15}N-αA_{red} sample (^{15}N-αA_{red}-IPSL) showed a substantial decrease (~40-50 %) in the peak intensity ratios between the paramagnetic

(oxidized) and diamagnetic (reduced) states (I_{para}/I_{dia}) for residues in the IPV region, such as A158, I159 and V161 (**Fig. 3e**).

If the observed PREs would be a consequence of random-coil like structural fluctuations of the CTD, PRE effects would localize around C142 (± 10 amino acids) (include reference: Dyson HJ, Wright PE (2004) Unfolded proteins and protein folding studied by NMR. Chem. Rev. 104: 3607-3622). We observe, however, a flat PRE profile with minimum intensity around A158, suggesting that CTD is either partially structured or exchanges between a bound and a free form. We can exclude the former interpretation as the CTD chemical shifts of oxidized and reduced spin-labeled αA-crystallin are rather similar (**Supplementary Fig. 6**).

Due to the high molecular weight of the αA-crystallin oligomers, no direct PREs can be measured for the CTR bound state. However, chemical exchange between bound and unbound CTRs allows to indirectly access the proximity of the CTD to the β4/β8 groove (include reference: Clore GM, Iwahara J (2009) Theory, Practice, and Applications of Paramagnetic Relaxation Enhancement for the Characterization of Transient Low-Population States of Biological Macromolecules and Their Complexes. Chem. Rev. 109: 4108-4139). The measured trPREs thus allow to probe intra- and intermolecular 3D domain-swapping.

To distinguish whether the unbound CTRs are in proximity of the ACD of the same protomer (non 3D domain-swapped similar) or an adjacent one (3D domain-swapped similar), we incubated spin-labelled ^{14}N-αA_{red} (^{14}N-αA_{red}-IPSL) with ^{15}N-αA_{red} in a 1:1 molar ratio (^{15}N-αA_{red}+^{14}N-αA_{red}-IPSL). In case all CTR interactions would involve 3D domain swapping, an attenuation of the signal intensity by 25 % would be expected. The fact, that only a decrease by 10-15 % in the peak intensity is observed (**Fig. 3f**) is in agreement with the cryo-EM results that indicate that ~20 % of the CTRs are in a 3D domain-swapped state (**Supplementary Table 2**). Both experiments thus imply that the 3D domain-swapped state is not dominantly populated in the oligomer ensemble of reduced αA-crystallin.

In vitro formation of an intramolecular disulfide bond in human αA-crystallin

In agreement with the literature, we detected in an Ellman`s assay on αA_{red} 0.93 ± 0.008 mol (SH) / mol (protein) corresponding to one accessible cysteine residue. The presence of only one reactive cysteine is puzzling, considering that the cysteines C131 and C142 of human αA-crystallin form an intramolecular disulfide bridge *in vivo*[34-37].

In our pseudo-atomic model of αA_{red}, the cysteines are located on adjacent antiparallel β8- and β9-strands and point in opposite directions (**Fig. 3d**). Their C_α atoms are ~6 Å apart, which is within the C_α-C_α distance range of 3.8 Å – 6.8 Å usually observed for disulfide bond conformations in proteins, but farther than the mean C_α-C_α distance of ~4.6 Å found in cross-strand disulfides[44]. The formation of a cross-strand disulfide bond between C131 and C142

would require the rotation of the cysteine side chains towards each other, resulting in significant conformational changes upon oxidation of αA-crystallin.

To study the formation of an intramolecular disulfide bond in αA-crystallin, we performed redox titrations with glutathione (**Fig. 4**). At -149 mV, roughly 50 % of the protein was oxidized to the intramolecularly cross-linked species (αA_{ox}), the remaining fraction consisted of intermolecularly disulfide-linked dimers (~20%) and trimers (~14%) (**Fig. 4a**). Upon quantification of the ratio of αA_{red} and αA_{ox} monomer bands, the equilibrium constant of the redox reaction for intramolecular disulfide bond formation K_{eq} was determined to be 0.434 mM corresponding to a redox potential of the intramolecular disulfide of -135 mV (**Fig. 4c**). We also performed the titration reactions with $\alpha A_{ox.}$ (**Fig. 4b,e**). The results indicated that after 20 h, the forward and reverse reactions were indistinguishable and the thermodynamic equilibrium was reached (**Fig, 4c,f**).

For comparison, the above value is between the redox potentials of the catalytic disulfides in bacterial DsbA and DsbC, oxido-reductases with a strained conformation in the oxidized state[45,46]. The low reaction rate and the formation of a substantial amount of intermolecularly disulfide-bridged species suggest a thermodynamically unfavorable conformational state for intramolecular disulfide formation also in the case of αA-crystallin. Thus, a denaturant should facilitate oxidation. Indeed, in the presence of urea, the disulfide-linked oligomers were abolished and half-maximal oxidation was achieved at -222 mV (**Fig. 4d,f**). In the presence of urea, we also detected 1.92 ± 0.070 mol (SH) / mol (protein) for αA_{red}, implying that destabilization leads to the accessibility of both cysteines.

Structural impact of the intramolecular disulfide bond on human αA-crystallin

Circular dichroism (CD) spectroscopy showed that oxidation does not lead to pronounced changes in the secondary structure (**Supplementary Fig. 7a**). However, differences became apparent in the environment of phenylalanine/tyrosine and tryptophan residues (**Supplementary Fig. 7b**). Since ~60% of the Phe and Tyr residues as well as the single Trp are located within the NTR, altered tertiary interactions within the NTR upon oxidation appeared likely.

Electron micrographs of negatively-stained αA_{ox} revealed that the protein assembles into oligomers that are more polydisperse and larger than observed for αA_{red} (**Fig. 5a**). The average oligomer size shifted from ~13.5 nm for αA_{red} to ~17.7 nm for αA_{ox} (**Fig. 5b**). In agreement, SEC experiments indicated an increase in molecular mass from 380 kDa for αA_{red} to 770 kDa for αA_{ox} (**Supplementary Fig. 7c**) and sedimentation velocity aUC experiments showed an increase in the sedimentation coefficient ($<s_{20,w}>$) from 14 S[19] to 25 S (**Supplementary Fig. 7d**).

The projections seen in electron micrographs of negatively-stained αA_{ox} particles are either round or slightly elongated (**Fig. 5a**) and resemble projections seen in αA_{red} samples. A preliminary 3D-reconstruction of a 32-mer calculated from few class averages including 1,500 single particle images (**Supplementary Fig. 7e**) without employing any starting model revealed a hollow, slightly elongated assembly with D2 symmetry (**Fig. 5c and Supplementary Fig. 7f**). Notably, the assembly contains the characteristic Z-shaped tetramers as seen in the oligomers of αA_{red} (**Fig. 1**), but it is expanded through the insertion of further building blocks apparently composed of dimers (**Fig. 5c**).

The overall architecture of αA_{ox} 32-mer implied altered residue and/or subunit proximities and consequently an altered cross-linking behavior compared to αA_{red}. Due to the lack of quantitative cross-linking data, we only tentatively compared both patterns in their most striking features. The comparison revealed a higher number of interactions in αA_{ox} (**Supplementary Table 4**) which included those observed for αA_{red} but also indicated differences between the two redox states. As such many cross-links observed only in αA_{ox} involved residues located within the NTR as well as within β4-, β6+7- and β9-strands (including K145) suggesting alteration of their relative positions and/or enhanced sidechain accessibilities upon oxidation (**Supplementary Fig. 4b**).

The intramolecular disulfide affects local structural dynamics of αA-crystallin

To further test how intramolecular disulfide formation affects the structure and dynamics of αA-crystallin, we performed hydrogen-deuterium exchange coupled to mass spectrometry (HDX-MS) (**Fig. 6a and Supplementary Fig. 8**). In agreement with previous studies[47], peptides from the NTR were characterized by a moderate protection at short D_2O exposure times, but became increasingly deuterated at longer exposure, consistent with the dynamic nature of this region sampling different conformations. The peptides from the ACD showed in general lower exchange. The β5- and β6+7-strands (F93-E102 and Y109-R119, respectively) were most strongly protected, while the CTR exchanged readily consistent with high exposure/flexibility. Thus, the degree of exchange in αA_{ox} was similar to that observed for αA_{red}, but specific differences existed. In αA_{ox}, the N-terminal stretch comprising residues D2-F10 exhibited increased protection. β6+7- (Y109-R119), the C-terminal region of the β8-strand (L133 and S134) and the β9-strand (L139-G143) as well as the loop connecting the latter became deprotected upon disulfide formation with F141 (β9-strand, neighboring C142) showing the strongest deprotection. These results suggest that the introduction of the intramolecular disulfide affects dynamics, solvent exposure and the hydrogen bonding network around the sites of disulfide formation (**Fig. 6b**).

To test oligomer stability, we performed aUC experiments in the presence of urea. With increasing urea concentrations, both αA_{red} and αA_{ox} oligomers dissociated successively. A

dissociated species with a sedimentation coefficient of 2 S was observed at 4.5 M urea for αA_{red}, and at 3.5 M urea for αA_{ox} (**Supplementary Fig. 9a**). Similarly, urea-induced unfolding transitions monitored by intrinsic fluorescence revealed cooperative unfolding with midpoints at 3.8 M and 2.7 M urea for αA_{red} and αA_{ox}, respectively (**Supplementary Fig. 9b**).

Chaperone activity of oxidized αA-crystallin

To compare αA_{red} and αA_{ox} functionally, we performed *in vitro* aggregation assays using p53 and MDH as model substrates and assessed the redox states of αA-crystallin and the model substrates. For comparison, we performed the same experiments in the presence of GSSG and the reduced and oxidized forms of DsbA. The heat-induced aggregation of p53 was efficiently suppressed only in the presence of αA_{ox} (**Fig. 7a**). Remarkably, when αA_{ox} was present, disulfide-linked large oligomers of p53 were formed and concomitantly αA_{red} appeared (**Fig. 7b**) indicating that the disulfide in αA_{ox} was transferred to p53. Interestingly, when we added $DsbA_{ox}$, only a slight aggregation suppression activity was detected (**Fig. 7a**). However, also in this case, high molecular weight disulfide-bonded p53 aggregates were formed (**Fig. 7b**) at a rate similar to that observed for αA_{ox} (**Fig. 7c**). These results indicate that αA_{ox} and $DsbA_{ox}$ share the ability to transfer their disulfide bond to destabilized p53. The addition of GSSG neither suppressed aggregation, nor did it lead to the formation of disulfide-linked species (**Fig. 7a,b**). Such species were also absent when αA_{red} or $DsbA_{red}$ were present (**Supplementary Fig. 10a**).

Both αA_{red} and αA_{ox} suppressed the heat-induced aggregation of MDH (**Supplementary Fig. 10b**). As in the case of p53, αA_{ox} transferred its intramolecular disulfide almost quantitatively to MDH resulting in intermolecularly cross-linked MDH species (**Supplementary Fig. 10c,d**). In the presence of $DsbA_{ox}$, the MDH monomer band disappeared (**Supplementary Fig. 10c**), but disulfide-bonded oligomers were not detected possibly due to their large size (**Supplementary Fig. 10d**). In the presence of GSSG or $DsbA_{red}$, the aggregation kinetics of MDH was similar to the control and no cross-linked MDH species were observed (**Supplementary Fig. 10b,d,e**).

Taken together, the above results demonstrate that αA_{red} and αA_{ox} differ in their *in vitro* chaperone activities towards model substrates and αA_{ox}, similar to DsbA, is capable of transferring its disulfide bond to destabilized model substrates.

Discussion

Human αA-crystallin exists in heterogeneous ensembles of oligomers of varying subunit stoichiometries. The atomic models determined by combining data from cryo-EM, X-ray crystallography, NMR and molecular modeling reveal the roles of the NTR and CTR in oligomerization and C-terminal domain swapping as a determinant of ensemble heterogeneity. The recurring unit of αA_{red} oligomers is a tetramer in which two β7-interface dimers associate at the equator of the barrel-shaped assembly through N-terminal interactions. Further N-terminal interactions at the poles mediate the formation of higher-order assemblies by linking tetrameric units. A tetrameric building block is consistent with previous studies[20-23].

The homology-modeled structure of the NTR contains 3 short helices connected by flexible loops consistent with the propensity of NTRs to adopt secondary structure elements[29,48]. These regions are highly dynamic and exist as ensembles of heterogeneous conformations[29,49,50]. In αA-crystallin, even the protomers in the apical and equatorial regions of the same oligomer possess different conformations. In our model, representing one of several possibilities, the N-terminal interactions occur mainly between the loops connecting helices α2 and α3. The amphiphatic helix α2 (residues 20-27) covering the conserved phenylalanine-rich sequence RLFDQXFG[14] dictates the position of the interacting loop regions in equatorial protomers. This motif was implicated to contribute to the higher order subunit assembly, oligomer stability and dynamics[51].

The CTR of αA_{red} occurs in non-3D and 3D domain-swapped configurations as previously captured in crystals of truncated forms of zebrafish[16] and bovine αA-crystallin[15], respectively. Our study demonstrates that both configurations coexist in solution. The transition between the two states requires the dissociation of the IPV motif from the β4/β8 groove. However, NMR studies on human αB-crystallin[52] and Hsp27[53] show that the IXI motif is highly dynamic in solution and not rigidly bound to the protein scaffold. In αA-crystallin, the enhanced dynamics of the CTR is likely to facilitate domain swapping.

In human αA-crystallin, the interplay between the geometric constraints imposed by the assembly architecture and the hinge loop connecting the CTR to the ACD is very likely to dictate the propensity for domain swapping. The three αA-crystallin assemblies investigated differ in their number of subunits but possess similar dimensions. As a consequence, in oligomers with a higher number of subunits, the protomers are packed more closely, i.e. inter-protomer distances decrease gradually from 12-mer to 20-mer. In all three assemblies, distance constraints preclude intermolecular binding of the CTR in apical protomers. However, the interactions between equatorial protomers vary with oligomer size: In equatorial protomers of the 12-mer, the non-3D domain-swapped configuration is favored as a flexible chain of a given length is less likely to span large distances relative to its own length, which results in

folding back of the chain on itself, adopting the non-3D domain-swapped configuration. Shorter distances promote domain swapping, as it occurs in all equatorial protomers of the 20-mer population. In the 16-mer population, both configurations coexist, nevertheless, the domain-swapped state might impose more strain on the hinge region, and in consequence, is less favored.

Despite the high similarity at the sequence level and approximately the same monomer length, αA- and αB-crystallin form different geometric bodies utilizing the same type of interactions: the β7-interface mediates dimerization and oligomerization is supported by N-terminal interactions, as well as by IXI-binding to the neighboring protomer. Nevertheless, the importance of the CTR differ: while the CTR plays a decisive role in the formation of hexameric species of human αB-crystallin[54,55], the CTR of human αA-crystallin contributes to the formation of higher-order oligomers only in the 3D domain-swapped form. N-terminal interactions are key to oligomer formation for all assembly types. The 12-meric species, the most abundant oligomer population, assembles without participation of the CTR in intermolecular interactions indicating that there is no stringent contribution of the IXI motif to oligomer formation. Consistent with this, both human[56] and bovine[57] αA-crystallin retain their ability to oligomerize upon mutations of their IXI motifs or its deletion[24]. This indicates the ability of αA-crystallin to form different types of oligomeric assemblies using different subunit interfaces without the participation of its IPV motif.

Oxidized αA-crystallin is highly abundant in young lenses without interfering with lens transparency[36]. The oxidation of αA-crystallin *in vitro* requires the presence of destabilizing agents which leads to the dissociation of oligomers. This suggests that local conformational changes and/or partial unfolding occur, putting the two cysteines in the β8- and β9-strands in an appropriate spatial proximity while preserving the “basic” ACD fold. It has been suggested that partial unfolding of monomers upon dissociation may be a common property of human sHsps and partly unfolded monomers may exist within larger oligomers[58,59]. Upon removal of urea, αA_{ox} reassembles into oligomers that are distinct from those of αA_{red} harboring subunits which are locally more dynamic in their β6+7-, β8- and β9-strands.

The redox potential of the intramolecular disulfide bridge in human αA-crystallin is comparable to that determined for thiol-disulfide oxido-reductases[45,60]. In the presence of urea, the intramolecular disulfide is formed at -220 mV, which is even below the estimated redox potentials of approximately -204 mV and -217 mV at the nuclear and cortical regions, respectively, of the young lens[61,62], thus enabling the formation of the intramolecular disulfide bridge *in vivo.* Although it is delicate to deduce the redox potential of a disulfide bond *in vivo* from the redox potential determined *in vitro* under equilibrium conditions in dilute solutions, the mere existence of the intramolecular disulfide in αA-crystallin *in vivo* hints at certain similarities of its redox properties *in vitro* and *in vivo*.

The intramolecular disulfide bridge in human αA-crystallin is a cross-strand disulfide. These are thought to be reactive redox-based conformational switches due to the strain introduced into the disulfide bond[63]. Although the edge strand β8 might tolerate the conformational changes/distortions caused by the disulfide bond to a certain extent, the diminished stability of αA_{ox} against urea-induced dissociation and unfolding compared to αA_{red} is in support of a strained structure.

Interestingly, the two cysteines in human αA-crystallin are conserved among species with increased life span, e.g. primates. *In vivo*, introduction of additional cysteine residues seems to be detrimental, as naturally occurring arginine to cysteine mutations of human αA-crystallin are all associated with cataract[5]. Together with the evolutionary selection against cysteines in general, this suggests that the cysteines of human αA-crystallin must serve a function in the eye lens. This appears contradictory to the increase of intramolecular disulfides concomitant with a decrease in chaperone activity of αA-crystallin during ageing and cataractogenesis[42]. It should, however, be noted that only the coincidence of these processes has yet been demonstrated, but not a direct causality between them. The precise relationship between cysteine oxidation and cataractogenesis needs to be further clarified.

αA_{ox} is able to transfer its intramolecular disulfide to destabilized substrates, i.e. it has redox properties intermediate between disulfide oxidases DsbA and DsbC. αA-crystallin may thus be an important component in the lenticular redox network. Given that it constitutes roughly ~15-20 % of the eye lens protein, this corresponds to an intracellular concentration of 3-4 mM. The lenticular glutathione concentration is in the order of ~3.7 mM in the outer cortical regions and ~2.8 mM in the nuclear regions in young lenses[62,64]. It is therefore likely that the redox state of the eye lens is not solely dictated by the glutathione system, but αA-crystallin itself will be an integral co-determinant of the lenticular redox system. It is tempting to speculate that αA-crystallin might be a yet unknown player in lenticular redox homeostasis. It could well be that the preferential oxidation of αA-crystallin prevents the formation of nonnative disulfide bonds in other crystallins and thus their aggregation in the eye lens. Further *in vivo* studies are required to address this issue.

Taken together, our structural analysis of αA-crystallin revealing the design principles of its defined ensembles of oligomers together with the differences between αA_{red} and αA_{ox} provides a framework for understanding its role in the normal lens and in cataractogenesis.

Online Methods

Cloning and protein purification

Wild-type human αA-crystallin was cloned into the pET28b(+) expression plasmid as described previously[19]. The expression plasmid was transformed into the *Escherichia coli* expression strain BL21-CodonPlus(DE3)-RIL (Agilent Technologies, Santa Clara, CA, USA). Cells were grown in LB_{kan} at 37°C until an OD_{600} of ~1.5 was reached. The culture was chilled to 20°C and protein expression was induced by the addition of 1 mM isopropyl β-D-1-thiogalactopyranoside (IPTG, Serva, Heidelberg, Germany). After 16 h of incubation, the cells were harvested by centrifugation at 7,000 x g for 10 min and resuspended in disruption buffer 50 mM Tris/Acetate pH 9.0, 1 mM EDTA, 1 mM dithiothreitol (DTT), 1 x protease inhibitor mix G (Serva, Heidelberg, Germany). After cell lysis using a basic Z cell disruptor system (Constant Systems, Northants, UK) at 2.3 kbar cooled to 12 °C, the lysate was cleared by centrifugation at 20,000 x g for 45 min at 6 °C. The cleared lysate was applied to a Q-Sepharose FF anion exchange column (50 mL bed volume) previously equilibrated with 20 mM Tris/Acetate pH 9.0, 10 mM KCl, 1 mM EDTA, 1 mM DTT. Protein was eluted by running a gradient to 1 M KCl in equilibration buffer. Fractions containing αA-crystallin were pooled and dialyzed against 10 mM MES/KOH pH 6.0, 10 mM KCl, 1 mM ETDA, 1 mM DTT. After dialysis, urea was added to 4.5 M final concentration. The protein solution was passed over an SP-Sepharose FF cation exchange column (50 mL bed volume) equilibrated in 10 mM MES/KOH pH 6.0, 10 mM KCl, 1 mM ETDA, 1 mM DTT, 4.5 M urea and eluted by a gradient to 10 mM MES/KOH pH 6.0, 1 M KCl, 1 mM ETDA, 1 mM DTT, 4.5 M urea. αA-crystallin containing fractions were pooled, concentrated and applied to a HiLoad Superdex 75 PG gel filtration column pre-equilibrated with 20 mM Tris/Acetate, pH 8.5, 1 mM EDTA, 1 mM DTT, 4.5 M urea. A subsequent high-resolution anion exchange chromatography step was performed using a Resource Q 6 ml column and an elution gradient 0-10 mM KCl in 20 mM Tris/Acetate, pH 8.5, 1 mM EDTA, 1 mM DTT, 4.5 M urea. The protein was refolded by dialysis against PBS (137 mM NaCl, 2.7 mM KCl, 8.1 mM Na_2HPO_4, 1.76 mM KH_2PO_4, pH 7.4), 1 mM EDTA, 1 mM DTT and concentrated using an Amicon stirred concentrator cell (10.000 MWCO, Merck Millipore, Darmstadt, Germany). As a final polishing step, a gel filtration run on a HiLoad Superdex 200 PG column equilibrated in PBS, 1 mM EDTA, 1 mM DTT was performed. The procedure yielded $αA_{red}$ preparations of > 95% homogeneity as judged by SDS-PAGE. Aliquots of the purified protein were stored at -80 °C in gel filtration buffer. Prior to all experiments, protein aliquots were thawed and incubated for 3 h at 37 °C to ensure proper thermal equilibration. If not stated otherwise, all experiments were performed in PBS buffer, 1mM EDTA, with either 1 mM DTT or 1 mM trans-4,5-dihydroxy-1,2-dithiane (DTT_{ox}) present. For experiments in which reductants or oxidants were likely to interfere, the buffer was exchanged to thoroughly degassed and N_2-purged PBS, 1 mM EDTA

using 7K MWCO polyacrylamide desalting columns (Thermo Scientific, Waltham, MA, USA) to remove residual DTT.

Redox titration, preparative protein oxidation and Ellman's assay

Redox titrations were performed according to Wunderlich & Glockshuber[45]. To rule out a potential interference of O_2 from air during redox titrations, the water used for the preparation of buffer was thoroughly degassed and purged with N_2 over night. Pipetting steps and incubation for equilibration were carried out in an anaerobic chamber (Coy laboratory products, Grass Lake, MI, USA) under N_2/H_2 (98%/2%) atmosphere. All solutions were transferred into the anaerobic chamber immediately after preparation in N_2-purged water. All reagents and tubes were stored in the anaerobic chamber at least 24 h before the start of the experiment. Initially, the storage buffer of αA_{red} was exchanged to PBS, 1 mM EDTA using gel filtration spin columns, the protein was transferred to the anaerobic chamber and diluted (10 µM final concentration) into buffers of a specified redox-potential as defined by a mixture of oxidized and reduced glutathione, GSSG and GSH, respectively, in PBS, 1 mM EDTA. The total concentration of glutathione monomers was kept at 5 mM for all reactions. After equilibration for 20 h at 43 °C, disulfide exchange was quenched by the addition of 25 mM N-ethyl-maleimide (NEM, dissolved in dry ethanol) and incubation for 20 min at 20°C. For redox-titrations in the presence of urea, all redox buffers and the buffer for initial DTT removal contained 4.5 M urea. The quenched reactions were analyzed by loading 1 µg of total protein per lane onto gradient gels (TG Prime, 8-16%, Serva, Heidelberg, Germany) using non-reducing sample buffer. The relative amount of remnant reduced and oxidized monomeric αA-crystallin (*R*) was quantified by densitometry using ImageJ. The equilibrium constant for the formation of the intramolecular disulfide K_{eq} was determined through nonlinear regression of the data using the function $R = ([GSH]^2/[GSSG])/(K_{eq} + ([GSH]^2)/[GSSG])$. The K_{eq} obtained (4.34×10^{-4} M for the reaction of αA_{red} under native conditions and 0.257 M for the reaction of αA_{red} in the presence of urea and 0.306 M for the reaction of αA_{ox} in the presence of urea) were used to determine the corresponding redox potential at 43 °C and pH 7.4 from the Nernst equation $E_{0\,\alpha A} = E_{0\,GSH/GSSG} - (RT/nF) \times \ln K_{eq}$ with $E_{0\,GSH/GSSG} = -240\,mV$, which is the standard potential for the glutathione redox pair at 40 °C and pH 7.4[65]. To assess the reversibility of the reaction, the titrations were equivalently performed using αA_{ox}. The data for αA_{ox} were processed as for αA_{red}.

To produce preparative amounts of αA_{ox}, protein at a concentration of 50 µM was subjected to buffer exchange using a HiPrep 26/10 desalting column (GE Healthcare) equilibrated in PBS, 1 mM EDTA, 4.5 M urea. Subsequently, the eluting protein was brought to 37 °C, supplemented with 2.5 mM GSSG and 5 µM GSH, and incubated for 6 h at 37 °C. After incubation, the redox system was removed by exchanging the buffer to PBS, 1 mM EDTA, 4.5

M urea. The eluate was then dialyzed twice against 5 L of PBS, 1 mM EDTA. The oxidation state of the protein was validated after quenching with NEM by non-reducing SDS-PAGE.
The Ellman's assay was performed according to Simpson, 2008[66]. The reaction was scaled to 100 µL volume and the final protein concentrations in the reaction mixture were 26 µM for αA_{red} and 22 µM for αA_{ox}.

Quaternary structure analysis

***Analytical gel filtration (SEC)* –** For analytical gel filtration, 10 µl of the protein sample at a concentration of 10 µM were loaded onto a Superose 6 10/300 GL (GE Healthcare, Chalfont St Giles, UK). The gel filtration runs were carried out at 20°C using PBS, 1 mM EDTA as a running buffer at a flow rate of 0.5 mL/min. Proteins were detected by fluorescence at an excitation (Ex) wavelength of 295 nm and an emission (Em) wavelength of 335 nm. The gel filtration standard (Bio-Rad, Hercules, CA, USA) was used for calibration.

***Analytical ultracentrifugation (aUC)* –** Sedimentation velocity analytical ultracentrifugation (SV-aUC) experiments were performed on a ProteomeLab XL-I analytical ultracentrifuge (Beckman Coulter, Brea, CA, USA) equipped with UV/VIS absorbance optics. For the experiments, 400 µl of a 20 µM protein solution and 450 µl of the reference buffer solution were loaded into 12 mm double-sector epon-filled centerpieces, covered with quartz windows. For αA_{ox} samples, Dulbecco's PBS, 1 mM EDTA was used. For αA_{red} samples, 1 mM DTT was added to the buffer.
Samples were pre-incubated at 37 °C for 3 hours to ensure thermal equilibrium and subsequently centrifuged at 34,000 rpm using an An-50 Ti rotor (Beckman Coulter, Brea, CA, USA) at 20 °C. For urea titration experiments, αA-crystallin stock solution was diluted after incubation for 3 h at 37 °C to give a working concentration of 20 µM at the indicated concentrations of urea. Radial absorbance scans were acquired continuously at 280 nm with a radial step size of 0.003 cm until complete sedimentation of the sample, with an average duration of 75 seconds per scan. For concentration titration experiments, the detection wavelength was adjusted to 230 nm in the concentration range from 2 - 10 µM and to 290 nm from 10 - 150 µM protein, respectively. To ensure data comparability, the 10 µM αA-crystallin samples were measured at both wavelengths.The resulting sedimentation velocity profiles were analyzed with the d*c*/d*t* method[67] and normalized to s(20,w). The buffer density (ρ) and buffer viscosity (η) used for data analysis was calculated with SEDNTERP (BITC, University of New Hampshire, NH; USA).

***Negative stain electron microscopy (NS-EM)* –** Negative staining experiments were conducted as described previously[19]. Data were recorded on a JEOL JEM-1400 Plus transmission electron microscope (Jeol, Tokyo, Japan) operated at 120 kV. For the analysis

of particle size distributions, single particle images were extracted from micrographs of negatively stained samples using „e2boxer“ of the EMAN software package[68]. The images were centered, band-pass filtered and subjected to multivariate statistical analysis (MSA) within the IMAGIC suite[69]. The particles were classified using all eigenvectors characterizing size heterogeneity. Oligomer sizes were determined as diameters of circumscribing circles of the class averages using ImageJ.

Extrinsic and intrinsic fluorescence and circular dichroism (CD) spectroscopy

To assess protein stability, urea-induced unfolding equilibria were determined in dependence of the urea concentration by intrinsic fluorescence measurements. Unfolding mixtures contained 4 µM of protein and the indicated amount of urea dissolved in degassed, N_2-purged PBS, 1 mM EDTA with 1 mM DTT or DTT_{ox}. The concentration of urea was verified by refractive index determination. Samples were incubated for 16 h. Spectra were measured in triplicates using a Jasco FP-6500 spectrofluorimeter (Jasco, Tokyo, Japan) connected to a thermostat. Hellma QS 10mm x 2 mm fluorescence ultra-micro cuvettes (Hellma, Müllheim, Germany) were used for fluorescence measurements. The excitation wavelength was set to 295 nm and emission spectra were recorded from 305 nm to 450 nm. During incubation and measurement, the samples were kept at 20 °C. The acquired spectra were corrected for the corresponding buffer signal. For each spectrum, at a given concentration of urea (denoted as [*urea*]), the intensity averaged emission wavelength $\langle\lambda\rangle_{[urea]}$ was calculated[70]. The fraction of natively folded protein (f_{folded}) was calculated for the measurement range between 0 M urea and 7.5 M urea as $f_{folded} = \langle\lambda\rangle_{(7.5M\ urea)} - \langle\lambda\rangle_{[urea]} / \langle\lambda\rangle_{(7.5M\ urea)} - \langle\lambda\rangle_{(0M\ urea)}$ and plotted versus denaturant concentration.

Circular dichroism (CD) spectra in the near (250-320 nm) and far (200-260 nm) UV-range were measured using a Jasco J-710 (Jasco, Tokyo, Japan) or a Chirascan (Applied Phostophysics, Leatherhead, United Kingdom) circular dichroism spectrophotometers equipped with a thermostated cuvette holder set to 20 °C. Near-UV CD spectra were recorded at a protein concentration of 100 µM, far-UV CD spectra were measured at 40 µM in 20 mM KH_2PO_4/KOH, pH 7.4, 1 mM EDTA. To record near-UV spectra, a QS 1 cm cuvette was used, for far-UV spectra a detachable window QS 0.2 mm cuvette (both Hellma, Müllheim, Germany).

Hydrogen/Deuterium exchange–mass spectrometry (H/DX-MS)

H/DX experiments were performed using an ACQUITY UPLC M-class system with HDX technology (Waters, Milford, MA, USA). H/DX kinetics were determined by measuring data points at 0, 10, 60, 600 and 1800 s exposure to deuterated buffer at 20°C. At each data point, 4 µl of a solution of 30 µM protein were diluted automatically 1:20 into PBS, 1 mM EDTA, 1 mM DTT or 1mM trans-4,5-dihydroxy-1,2-dithiane, pD 7.5, prepared with 99.9 % D_2O or H_2O

as reference buffer. The reaction mixture was quenched by the addition of 200 mM KH_2PO_4, 200 mM Na_2HPO_4, 4 M GdnHCl, 300 mM TCEP, pH 2.3 (titrated with HCl) in a ratio of 1:1 at 0 °C. 50 µl of the resulting sample were subjected to on-column peptic digest on an in-line Enzymate BEH pepsin column (2.1 x 30 mm) at 20°C. Peptides were trapped and desalted by reverse phase chromatography at 0° C using an Acquity UPLC C18 BEH VanGuard pre-column (1.7 µm C18 beads, 2.1 x 5 mm, Waters). For separation, an Acquity UPLC BEH C18 (1.7 µm, 1 x 100 mm) analytical column (Waters) at 0° C, and gradients with stepwise increasing acetonitrile (in 0.1 % formic acid) concentration from 5 – 35 % in 6 min, from 35 – 40 % in 1 min and from 40 – 95 % in 1 min were applied. The eluted peptides were analyzed using an in-line Synapt G2-Si QTOF HDMS mass spectrometer (Waters). MS data were collected over an m/z range of 100-2000. Mass accuracy was ensured by calibration with [Glu1]-Fibrinopeptide B (Waters) and peptides were identified by triplicate MS^E ramping the collision energy from 20-50 V. Data were analyzed using ProteinLynx Global Server (PLGS, Version 3.0.3) and DynamX (Version 3.0) software packages (Waters). As all samples were handled under identical conditions, deuterium levels were not corrected for back-exchange and were therefore reported as relative deuterium uptake levels. Briefly, for each peptide relative fractional exchange, is calculated dividing the deuterium level incorporated at a given timepoint (in Da) by the total number of backbone amide hydrogens in the peptide (this equals the number of amino acids, minus proline residues minus 1 for the N-terminal amide[71]. All experiments were performed with triplicate determination at each time point.

Aggregation assays

Chaperone assays and disulfide-transfer reactions were performed in parallel using malate dehydrogenase (MDH) or human p53 (p53) as model substrates in the absence of reductant. MDH was diluted to 4 µM and p53 was diluted to 2 µM into PBS containing 1 mM EDTA on ice. Oxidized and reduced αA-crystallin, oxidized and reduced DsbA and GSSG were added to a final concentration of 4 µM. The reaction mix was split in two aliquots. One of the aliquots was used to follow the aggregation of model substrates at 45 °C by recording the absorbance at 360 nm for 60-120 min using a Cary 50 UV/VIS spectrophotometer (Varian, Palo Alto, CA, USA) equipped with a temperature-adjustable cuvette holder. The other aliquot was used to withdraw samples at the indicated timepoints. One sample was withdrawn at t= 0 min for reference before starting the reaction by placement of the reaction mixtures to 45 °C in the photometer. The disulfide exchange reaction in every sample was quenched immediately after withdrawal by the addition of NEM to 25 mM final concentration. After 20 min of incubation at 20 °C, non-reducing SDS-PAGE sample buffer was added, the sample was incubated at 95°C for 5 min and analyzed on an 8-16% gradient gel (TG Prime, Serva, Heidelberg, Germany).

Cryo-electron microscopy (Cryo-EM), image processing and 3D-reconstruction

Sample preparation, data collection – For the preparation of the cryo-EM samples, 4 µL of αA_{red} solution (0.3 mg/mL in PBS, 1 mM EDTA, 1 mM DTT, pH 7.4) were applied to glow-discharged Quantifoil R 2/1 holey carbon copper grids, incubated for 30 sec, blotted, and plunge-frozen in liquid ethane using a manual plunger. The samples were mounted into autoloader cartridges and transferred into a Titan Krios electron microscope (FEI) equipped with a K2 Summit direct detector (GATAN) and operated in energy-filtered transmission electron microscopy (EFTEM) mode at 300 kV. Automatic data acquisition was performed using the TOM toolbox[72]. 2334 movie images were collected at defocus values ranging from -1.2 µm to - 2.5 µm and at a nominal magnification of ×37,000 (1.35 Å per pixel) in "super-resolution mode" (0.675 Å per pixel). The movies were recorded at dose rates of 7 - 8 electrons per pixel per second, with exposure times of 0.37 - 0.27 s per frame and a target total dose of 25 - 36 electrons per square ångström. The frames were aligned, averaged and binned to a final pixel size of 1.35 Å per pixel. Well-separated particle images were selected manually and extracted into 200 X 200 pixel boxes using „e2boxer" of the EMAN software package[68]. Images were corrected for the contrast transfer function by phase flipping using Bsoft[73]. All subsequent image processing procedures were carried out within the IMAGIC suite[69].

Image processing and 3D-reconstruction – For the processing of the cryo-EM data, reference-free class averages were generated from 74,068 CTF-corrected and band-pass filtered (20 Å - 160 Å) single particle images. The class averages revealed almost spherical particles ranging in size between 6 and 16 nm as well as elongated ones with a maximum length of 14 nm. The presence of 2-, 3-, 4- and 5-fold symmetries in projection images together with the variation of particle dimensions and shapes suggested the presence of multiple structures of a similar barrel like architecture but of varying subunit stoichiometries. Based on this, three models each consisting of a bundle of „pillars" (3, 4 and 5 pillars compatible with 3-, 4- and 5-fold symmetries) were generated as starting references. Reference-free class averages were sorted into initial particle subsets based on particle diameter and symmetry. Within each subset, an initial 3D-reconstruction was calculated by projection matching cycles using the above "pillar-bundle" models as starting models. In a next step of data sorting, the three initial 3D-reconstructions were used as references to align and sort all single particle images of the cryo-EM data set into three final subsets in an iterative procedure. All particles were aligned independently by multi reference alignment (MRA) to each of the three reference structures. Within each of the three particle sets, multivariate statistical analysis (MSA) was applied to generate class averages. The Euler angles of the class averages were assigned by angular reconstitution (AR)[74]. Subsequently, classes that mismatched with the corresponding model reprojections were sorted out. This "purification" step by MSA/AR was repeated until all

remaining class averages agreed well with reference reprojections, resulting in three distinct particle subsets.

For 3D-reconstruction, the final class averages were refined iteratively by 6 rounds of MRA and AR using starting models generated from the input class averages of the respective set. For the refinement, single particle images of each class were aligned with the corresponding reprojection of the respective preliminary reference, while particles that were rotated by more than 9 degrees as well as the 10% of images with the lowest cross correlation coefficients were ignored. Euler angles of the class averages comprising the remaining particles were refined by AR and a new 3D-reconstruction was calculated, which served as a reference for the subsequent refinement cycle. During refinement, filtering of input and output images as well of the reference models changed in every iteration starting from 20 Å and ending at 7 Å to sequentially allow more details to affect the alignment. Class averages and 3D-reconstructions were masked with an adaptive soft edge mask unless when used for Fourier shell correlation (FSC) calculations.

For resolution determination, the "gold standard" 0.143 criterion was used[75]. FSCs were calculated between the final reconstructions of independently processed half sets using the FSC validation server (http://pdbe.org/fsc) within the PDBe (Protein Data Bank in Europe)[76]. 3D reconstructions and atomic models were rendered using UCSF Chimera[77].

3D sampling and classification – To analyze the conformational heterogeneity of human αA-crystallin oligomers, the particles from the final oligomer subsets were subjected to band pass filtering (140 Å - 10 Å), normalisation and 3D sampling[78] followed by 3D classification. Within each data set, 1,000 random 3D-reconstructions from randomly selected 1,000 projection images were generated (3D sampling of structure sub-ensembles). The 3D-reconstructions were analyzed by 3D MSA followed by clustering into 10 distinct sub-populations by 3D-classification using IMAGIC.

NMR spectroscopy

Sample preparation – αA_{red} was recombinantly expressed in M9 minimal medium containing $^{15}NH_4Cl$ (1.0 g/L) (CIL, Andover, MA, USA) and uniformly labelled ^{13}C-glucose (2 g/L) (CIL, Andover, MA, USA). Labelled protein was purified as described above. For solution-state NMR, purified proteins were dialyzed against 10 mM HEPES/KOH (pH 7.4), 2 mM DTT, 1 mM EDTA (DTT was absent when oxidized protein was investigated).

Solution-state NMR spectroscopy – Solution-state NMR experiments were carried out employing a Bruker Biospin Avance III spectrometer operating at a ^1H Larmor frequency of 950 MHz (22.3 T) using a CPTCI triple-resonance cryoprobe. All experiments were performed at 300 K in HEPES/KOH buffer containing 5% D_2O.

Spin labeling experiments - 3-(2-iodoacetamido)-proxyl (IPSL) (Sigma-Aldrich, St. Louis, MO, USA) (50 mM stock dissolved in DMSO) was used for the spin-label reaction. Before addition of a 5-fold molar excess of IPSL, the protein solution at a concentration of 500 µM was reduced by adding 2 mM DTT. The buffer was afterwards exchanged to 1 M Tris-HCl (pH 8.0), 200 mM NaCl using a protein desalting spin column (Thermo Scientific, Waltham, MA, USA). Following an overnight reaction in the dark at 4 °C, the IPSL-tagged protein was passed twice through a desalting spin column to remove all unreacted spin label and change the buffer to 10 mM HEPES/KOH (pH 7.4) and 1 mM EDTA. As previous studies have shown that only one cysteine residue is readily surface accessible in native αA-crystallin (most likely C142 [32,33]), and this is in agreement with our structural model, we suggest IPSL primarily attaches C142. Two different samples were employed, one sample consisting of ^{15}N-labelled αA-crystallin (^{15}N αA_{red}) with spin label 3-(2-iodoacetamido)-proxyl (IPSL) (Sigma-Aldrich, St. Louis, MO, USA) attached (^{15}N αA_{red}-IPSL) and the other one consisting of a 1:1 mixture of ^{15}N-labelled αA-crystallin (^{15}N αA_{red}) with unlabelled αA-crystallin bearing the spin label (^{14}N αAr_{ed}-IPSL). To prepare the "mixed" sample, ^{15}N-αAr_{ed} was added in the reaction mixture to ^{14}N-αA_{red}-IPSL in a 1:1 ratio, yielding a final concentration of 300 µM for each protein component. The mixed sample (^{15}N αA_{red}+^{14}N-αA_{red}-IPSL) was subsequently incubated for 4 hrs at 37 °C. In both samples, reduction of the protein-bound IPSL was achieved with a 10 molar excess of freshly prepared ascorbic acid in HEPES/KOH buffer to yield the diamagnetic species. The spectra have been recorded at a temperature of 27 °C and a pH of 7.4.

NMR Data analysis – NMR data acquisition and processing was done in TopSpin 3.2 (Bruker BioSpin Corp.). Data were analyzed using the CcpNmr analysis software (University of Cambridge, United Kingdom)[79]. Paramagnetic relaxation enhancements (PREs) arising from the spin label were determined using the ratio of peak intensities of the ^{1}H, ^{15}N-HSQC spectra obtained for the paramagnetic (oxidized) and the diamagnetic (reduced) state (I_{para}/I_{dia}), in the absence and presence of 10 molar equivalents of ascorbic acid. Peak volumes were extracted by box integration using in-house Python scripts. The experimental error was set to two times the standard deviation of the noise and the uncertainty of the T_1 values was estimated by 1.000 Monte Carlo runs. R_1 rates were determined by fitting decay curves by an exponential function.

Cross-linking and mass spectrometry

Sample preparation – For cross-linking experiments, bis(sulfosuccinimidyl)suberate (BS3) cross-linker (Thermo Scientific, Waltham, MA, USA) was freshly dissolved to a stock concentration of 129 mg/mL (226 mM) in PBS, 1 mM EDTA. The BS3 stock solution was serially diluted to achieve different molar cross-linker:αA-crystallin ratios. αA-crystallin was diluted to a final concentration of 33 µM in a total volume of 50 µl in PBS, 1mM EDTA and 16 µl of the BS3 stock solution or dilutions thereof were added upon continuous vortexing of the

protein solution. The reaction mixture was incubated at 20 °C for 1 h and subsequently quenched by the addition of 10 µl of freshly prepared saturated ammonium bicarbonate solution (2.7 M) in H_2O. After an additional incubation period of 1 h, sample loading buffer was added and 10 µg of total protein were applied to a 4-12 % NuPAGE gel (Thermo Scientific, Waltham, MA, USA). The gel was run at a constant voltage of 200 V using MOPS-SDS-running buffer (Thermo Scientific, Waltham, MA, USA) until the dye front reached the end of the gel. For both αA_{red} and αA_{ox}, excised gel bands corresponding to monomers at a BS3:αA-crystallin ratio of 450:1 were pooled to provide the monomer sample. The dimer sample contained the dimer bands at BS3:αA-crystallin ratios of 450:1and 900:1, while the oligomer sample contained higher-order oligomer bands at 450:1 ratio. The samples were digested with trypsin (Thermo Fischer Scientific), following previously established protocols[80]. Briefly, proteins were first reduced with 10 mM DTT (Sigma-Aldrich) for 30 min at 37°C in a shaker and alkylated with 55 mM iodoacetamide (IAA) (Sigma-Aldrich) for 20 minutes at room temperature, followed by trypsin digestion overnight at 37°C. Digested peptides were desalted using C18-StageTips[81,82] for LC-MS/MS analysis. Data on monomer, dimer and higher-order oligomer bands were acquired separately.

Mass spectrometry **–** LC-MS/MS analysis was performed using Orbitrap Fusion Lumos (Thermo Fisher Scientific) with a “high/high” acquisition strategy. The peptide separation was carried out on an EASY-Spray column (50 cm × 75 µm i.d., PepMap C18, 2 µm particles, 100 Å pore size, Thermo Fisher Scientific). Mobile phase A consisted of water and 0.1% v/v formic acid. Mobile phase B consisted of 80% v/v acetonitrile and 0.1% v/v formic acid. Peptides were loaded at a flow rate of 0.3 µL/min and eluted at 0.2 µL/min using a linear gradient going from 2% mobile phase B to 40% mobile phase B over 109 min, followed by a linear increase from 40% to 95% mobile phase B in 11 min. The eluted peptides were directly introduced into the mass spectrometer. MS data were acquired in the data-dependent mode with 3 s acquisition cycle. Precursor spectrum was recorded in the Orbitrap with a resolution of 120,000. The ions with a precursor charge state between 3+ and 8+ were isolated with a window size of 1.6 m/z and fragmented using high-energy collision dissociation (HCD) with collision energy 30. The fragmentation spectra were recorded in the Orbitrap with a resolution of 15,000. Dynamic exclusion was enabled with single repeat count and 60 s exclusion duration.

The mass spectrometric raw files were processed into peak lists using MaxQuant (version 1.5.3.30)[83], and cross-linked peptides were matched to spectra using Xi software (version 1.6.745)[84]. Search parameters were MS accuracy, 3 ppm; MS/MS accuracy, 10ppm; enzyme, trypsin; cross-linker, BS3; max missed cleavages, 4; missing mono-isotopic peaks, 2[84]; fixed modification, carbamidomethylation on cysteine; variable modifications, oxidation on methionine; fragments, b and y ions with loss of H_2O, NH_3 and CH_3SOH. FDR was estimated using XiFDR on 5% residue level[86].

Model building

Structural modeling of the human αA-crystallin 16-mer was based on structural models of dimeric αA-crystallin that were prepared by homology modeling on either the non-3D domain-swapped structure of truncated αA-crystallin (αA_{60-166}) from zebrafish (PDB 3N3E)[16] or on the 3D domain-swapped structure of bovine truncated αA-crystallin (αA_{59-163}) (PDB 3L1E)[15] using the program Modeller[87]. As the N-terminal residues (αA_{1-59}) were missing in both crystal structures, structural models of this segment were generated based on homology modeling using the protein structure prediction server I-Tasser[88]. The secondary structure of the structural model showed good agreement with consensus secondary structure predictions. Secondary structure predictions were performed using 15 different web-based programs based on different algorithms and source datasets. Some of these programs turn out categorial predictions on the secondary structure for each residue (helix, strand, coil), whereas others return probabilities for the formation of each secondary structure element. To obtain a value summarizing the results, the relative abundance of the prediction for helix, strand or coil was calculated for each residue across all categorial predictions. This fractional value was used to obtain an average together with predictions returning probabilities, weighting the prediction from each program equally.

Prior to the flexible fitting, the homology modeled ACD dimer structures were fitted as rigid bodies into the corresponding cryo-EM densities for the non-3D and the 3D domain-swapped cases, respectively, using the program colores of the Situs package[89]. This resulted in symmetric arrangements of the dimers in the densities which, however, did not completely fill the available cryo-EM density. In case of the 3D domain-swapped conformation, sterically allowed intermolecular binding of the C-terminal extensions was modeled such that the arrangement confirmed with the structure found in bovine αA-crystallin dimer at the equatorial contacts. Hence, the IPV motif in the C-terminal segment binds to the corresponding binding groove in the dimer on the opposite site of the equatorial plane (the distance at the poles is too large to form such intermolecular contacts and it was assumed that the IPV motif binds intramolecularly as in the zebrafish ACD-dimer structure). In case of the non-3D swapped structure, only intramolecular IPV motif binding was assumed for the entire oligomer. The N-terminal modeled segment (αA_{1-59}) was placed randomly in various sterically possible positions such that a covalent bond to the truncated ACD domains (to residue 60) was possible. This resulted in ~ 40 different random placements. The oligomers were energy minimized using the Sander module of the Amber software package (Amber16)[90] employing a distance-dependent dielectric constant (proportional 4 x distance). Energy minimization involved 1000 steps of steepest descend followed by 3000 steps of conjugated gradient minimization. Molecular dynamics (MD) flexible fitting to the target cryo-EM densities was started from energy-

minimized structures using the emap option in Sander[91]. Consecutive simulations of 0.5 ns at 200 K and 300 K were performed and the final structure was again energy minimized. During the flexible fitting simulations, distance constraints between C_α atoms within each ACD dimer and within a distance interval of 6-12 Å were included to keep the structures close to the reference start structures. For the N-terminal segments, intra-segment distance restraints were included to keep the structure close to the start structure but allowing unrestrained full adjustment relative to other parts of the structures. The intra- or intermolecular contacts of the IPV motif with the corresponding binding region were restrained to stay close to the reference placements in the starting structures. In order to keep the fitted models symmetric with respect to the spatial arrangement both within each dimer and between dimers, the option to penalize the difference between two distances implemented in the Sander module of the Amber package was employed. The option was applied to a subset of backbone distances within each dimer and between ACD dimers. The flexible fitting converged typically within less than 0.5 ns of MD simulation (no further change occurred upon prolongation of the simulation). For each of the initial placements of the N-terminal segments, the final flexibly fitted structure was evaluated based on RMSD, stereochemistry and cross correlation with respect to the cryo-EM density. Several solutions showed either significant portions of the structure placed outside the cryo-EM density or indicated sterical overlap (high force field energy) and were not further considered. The non-3D and 3D domain-swapped structures with low force field energy and best cross correlation to the cryo-EM density were selected as best representative solutions.
12- and 20-mer pseudo-atomic models were generated from the 16-mer models by fitting the respective tetramers into the cryo-EM density and subsequent symmetrization within Chimera.

Molecular Dynamics simulations of ACD domain dimer in oxidized and reduced forms

The homology modelled human truncated non-swapped αA-crystallin ($\alpha A_{60–166}$) domain dimer with the intramolecular binding of the IPV motif was used to perform comparative MD simulations in explicit solvent. In case of the oxidized form, the structure contained a disulfide link between C131 and C142. Both the reduced and the oxidized forms were solvated in explicit water (TIP3P water model)[92] and using the AMBER ff14SB force field[90]. First, each system was energy minimized using steepest descent and conjugated gradient method. The systems were heated up to 300K using a Langevin dynamics, while keeping all heavy atoms restrained to the positions in the start structure. These restraints were reduced in a step-wise manner over the next 250 ps. After equilibration for 50ns (without any restraints) each system was simulated for 200 ns in a free, unrestrained MD simulation under constant pressure (1bar) and temperature (300 K). The minimization was carried out on CPU using the MPI version of AMBER's pmemd routine[89], other simulations were run on our in-house GPU cluster using the CUDA version of pmemd.

Data availability

All relevant data are available from the corresponding authors upon request and/or included in the manuscript or Supplementary Information. The cryo-EM density maps of αA-crystallin 12-, 16- and 20-mer have been deposited in the EMBD under the entry IDs EMD-4895, EMD-4894 and EMD-4896. The mass spectrometry proteomics data have been deposited to the ProteomeXchange Consortium via the PRIDE partner repository with the dataset identifier PXD013587 (Reviewer account details: Username: reviewer16270@ebi.ac.uk, Password: M5wEHQEq). The ^{1}H, ^{15}N, ^{13}C chemical shifts of reduced αA-crystallin are available at the BioMagResBank with the accession number BMRB-27109.

Acknowledgements

We are grateful to Prof. Jürgen Plitzko (Max-Planck Institute for Biochemistry, Martinsried) for continuous advice and support with electron microscopy and critical discussions. We thank Marie-Lena Jokisch and Rosario Ciccone for technical assistance during initial experiments. This work was supported by grants from the Deutsche Forschungsgemeinschaft (SFB 1035) and CIPSM to J.B., B.R., M.Z. and S.W. Cross-linking/mass spectrometry work was supported by the Wellcome Trust (103139). The Wellcome Centre for Cell Biology is supported by core funding from the Wellcome Trust (203149).

Author contributions

C.J.O.K., J.B. and S.W. designed and conceived the research plan. C.P., B.R. and C.J.O.K. performed electron microscopy experiments and processed the data. C.J.O.K. carried out, with contributions from P.W.N.S., E.V.M. and M.H., the experiments for the biochemical and biophysical characterization of the studied system. M.S. and S.A. performed NMR experiments. M.S. and B.R. analysed the NMR data. J.Z. conducted cross-linking/mass spectrometry experiments. J.Z. and J.R. analysed the cross-linking data. M.Z. performed molecular dynamics simulations and model building. C.J.O.K., J.B. and S.W. wrote the manuscript with input from all authors.

Conflict of interest

The authors declare that they have no conflict of interest.

References

1. Bloemendal, H. et al. Ageing and vision: structure, stability and function of lens crystallins. *Prog. Biophys. Mol. Biol.* **86**, 407–485 (2004).
2. Clark, A. R., Lubsen, N. H. & Slingsby C. sHSP in the eye lens: crystallin mutations, cataract and proteostasis. *Int. J. Biochem. Cell. Biol.* **44,** 1687–1697 (2012).
3. Horwitz, J. α-Crystallin can function as a molecular chaperone. *Proc. Natl. Acad. Sci. USA* **89**, 10449–10453 (1992).
4. Horwitz, J. Alpha-crystallin. *Exp. Eye Res.* **76**, 145–153 (2003).
5. Graw, J. Genetics of crystallins: cataract and beyond. *Exp. Eye Res.* **88**, 173–189 (2009).
6. Oguni, M. et al. Ontogeny of alpha-crystallin subunits in the lens of human and rat embryos. *Cell Tissue Res.* **276**, 151–154 (1994).
7. Iwaki, T., Kume-Iwaki, A., Liem, R. K. H. & Goldman, J. E. αB-crystallin is expressed in non-lenticular tissues and accumulates in Alexander's disease brain. *Cell* **57,** 71–78 (1989).
8. Srinivasan, A. N., Nagineni, C. N. & Bhat, S. P. αA-crystallin is expressed in non-ocular tissues. *J. Biol. Chem.* **267**, 23337–23341(1992).
9. Gangalum, R. K., Horwitz, J., Kohan, S. A. & Bhat, S. P. αA-crystallin and αB-crystallin reside in separate subcellular compartments in the developing ocular lens. *J. Biol. Chem.* **287**, 42407–42416 (2012).
10. Datta, S. A. & Rao, C. M. Differential temperature-dependent chaperone-like activity of αA- and αB-crystallin homoaggregates. *J. Biol. Chem.* **274**, 34773–34778 (1999).
11. Reddy, G. B., Das, K. P., Petrash, J. M. & Surewicz, W. K. Temperature-dependent chaperone activity and structural properties of human αA- and αB-crystallins. *J. Biol. Chem.* **275**, 4565–4570 (2000).
12. Kumar, L. V., Ramakrishna, T. & Rao, C. M. Structural and functional consequences of the mutation of a conserved arginine residue in αA- and αB-crystallins. *J. Biol. Chem.* **274**, 24137–24141 (1999).
13. Caspers, G. J., Leunissen, J. A. & de Jong, W. W. The expanding small heat-shock protein family, and structure predictions of the conserved “α-crystallin domain”. *J. Mol. Evol.* **40,** 238–248 (1995).
14. de Jong, W. W., Caspers, G. J. & Leunissen, J. A. Genealogy of the α-crystallin – small heat-shock protein superfamily. *Int. J. Biol. Macromol*. **22**, 151–162 (1998).
15. Laganowsky, A. et al. Crystal structures of truncated alphaA and alphaB crystallins reveal structural mechanisms of polydispersity important for eye lens function. *Protein Sci.* **19**, 1031–1043 (2010).
16. Laganowsky, A. & Eisenberg, D. Non-3D domain swapped crystal structure of truncated zebrafish alphaA crystallin. *Protein Sci.* **19**, 1978–1984 (2010).

17. Bova, M. P., Ding, L. L., Horwitz, J. & Fung, B. K. Subunit exchange of αA-crystallin. *J. Biol. Chem.* **272**, 29511–29517 (1997).
18. Aquilina, J. A. et al. Subunit exchange of polydisperse proteins: mass spectrometry reveals consequences of αA-crystallin truncation. *J. Biol. Chem.* **280**, 14485–1449 (2005).
19. Peschek, J. et al. The eye lens chaperone α-crystallin forms defined globular assemblies. *Proc. Natl. Acad. Sci. USA* **106**, 13272–13277 (2009).
20. Merck, K. B., de Haard-Hoekman, W. A., Essink, B. B. O., Bloemendal, H. & de Jong, W. W. Expression and aggregation of recombinant αA-crystallin and its two domains. *Biochim. Biophys. Acta* **1130**, 267–276 (1992).
21. Bova, M. P., Mchaourab, H. S., Han, Y. & Fung, B. K. K. Subunit exchange of small heat shock proteins. Analysis of oligomer formation of αA-crystallin and Hsp27 by fluorescence resonance energy transfer and site-directed truncations. *J. Biol. Chem.* **275**, 1035–1042 (2000).
22. Salerno, J. C., Eifert, C. L., Salerno, K. M. & Koretz, J. F. Structural diversity in the small heat shock protein superfamily: control of aggregation by the N-terminal region. *Protein Eng.* **16**, 847–851 (2003).
23. Kundu, M., Sen, P. C. & Das, K. P. Structure, stability, and chaperone function of αA-crystallin: role of N-terminal region. *Biopolymers* **86**, 177–192 (2007).
24. Andley, U. P., Mathur, S., Griest, T. A. & Petrash, J. M. Cloning, expression, and chaperone-like activity of human αA-crystallin. *J. Biol. Chem.* **271**, 31973–31980 (1996).
25. Thampi, P. & Abraham, E. C. Influence of the C-terminal residues on oligomerization of αA-crystallin. *Biochemistry* **42**, 11857–11863 (2003).
26. Rajan, S., Chandrashekar, R., Aziz, A. & Abraham, E. C. Role of arginine-163 and the ^{163}REEK^{166} motif in the oligomerization of truncated α-crystallins. *Biochemistry* **45**, 15684–15691 (2006).
27. Aziz, A., Santhoshkumar, P., Sharma, K. K. & Abraham, E. C. Cleavage of the C-terminal serine of human αA-crystallin produces αA_{1-172} with increased chaperone activity and oligomeric size. *Biochemistry* **46**, 2510–2519 (2007).
28. Treweek, T. M., Rekas, A., Walker, M. J. & Carver, J. A. A quantitative NMR spectroscopic examination of the flexibility of the C-terminal extensions of the molecular chaperones, αA- and αB-crystallin. *Exp. Eye Res.* **91**, 691–699 (2010).
29. Kim, K. K., Kim, R. & Kim, S. H. Crystal structure of a small heat-shock protein. *Nature* **394**, 595–599 (1998).
30. van Montfort, R. L., Basha, E., Friedrich, K. L., Slingsby, C. & Vierling E. Crystal structure and assembly of a eukaryotic small heat shock protein. *Nat. Struct. Biol.* **8**, 1025–1030 (2001).

31. Runkle, S., Hill, J., Kantorow, M., Horwitz, J. & Posner, M. Sequence and spatial expression of zebrafish (*Danio rerio*) αA-crystallin. *Mol. Vis.* **8**, 45–50 (2002).
32. Augusteyn, R. C., Hum, T. P., Putilin, T. P. & Thomson, J. A. The location of sulphydryl groups in α-crystallin. *Biochim. Biophys. Acta* **915**, 132–139 (1987).
33. Srikanthan, D., Bateman, O. A., Purkiss, A. G. & Slingsby, C. Sulfur in human crystallins. *Exp. Eye Res.* **79**, 823–831 (2004).
34. Miesbauer, L. R. et al. Post-translational modifications of water-soluble human lens crystallins from young adult. *J. Biol. Chem.* **269**, 12494–12502 (1994).
35. Takemoto, L. J. Oxidation of cysteine residues from alpha-A crystallin during cataractogenesis of the human lens. *Biochem. Biophys. Res. Commun.* **223**, 216–220 (1996).
36. Takemoto, L. J. Increase in the intramolecular disulfide bonding of alpha-A crystallin during aging of the human lens. *Exp. Eye Res.* **63**, 585–590 (1996).
37. Hains, P. G. & Truscott, R. J. W. Proteomic analysis of the oxidation of cysteine residues in human age-related nuclear cataract lenses. *Biochim. Biophys. Acta.* **1784**, 1959–1964 (2008).
38. Fan, X. et al. Evidence of highly conserved β-crystallin disulfidome that can be mimicked by *in vitro* oxidation in age-related human cataract and glutathione depleted mouse lens. *Mol. Cell. Proteomics* **14**, 3211–3223 (2015).
39. Yang, Z., Chamorro, M., Smith, D. L. & Smith, J. B. Identification of the major components of the high molecular weight crystallins from old human lenses. *Curr. Eye Res.* **13**, 415–421 (1994).
40. Lund, A. L., Smith, J. B. & Smith, D. L. Modifications of the water-insoluble human lens α-crystallins. *Exp. Eye Res.* **63**, 661–672 (1996).
41. Hanson, S. R. A., Hasan, A., Smith, D. L. & Smith, J. B. The major in vivo modifications of the human water-insoluble lens crystallins are disulfide bonds, deamidation, methionine oxidation, and backbone cleavage. *Exp. Eye Res.* **71**, 195–207 (2000).
42. Cherian-Shaw, M., Smith, J. B., Jiang, X. Y. & Abraham, E. C. Intrapolypeptide disulfides in human αA-crystallin and their effect on chaperone-like function. *Mol. Cell. Biochem.* **199**, 163-167 (1999).
43. Merkley, E. D. et al. Distance restraints from crosslinking mass spectrometry: Mining a molecular dynamics simulation database to evaluate lysine–lysine distances. *Protein Sci.* **23**, 747–759 (2014).
44. Chakraborty, K. et al. Protein stabilization by introduction of cross-strand disulfides. *Biochemistry* **44**, 14638–14646 (2005).
45. Wunderlich, M. & Glockshuber, R. Redox properties of protein disulfide isomerase (DsbA) from *Escherichia coli*. *Protein Sci.* **2**, 717–726 (1993).

46. Zapun, A., Missiakas, D., Raina, S. & Creighton, T. E. Structural and functional characterization of DsbC, a protein involved in disulfide bond formation in *Escherichia coli. Biochemistry*. **34**, 5075-89 (1995).
47. Hasan, A., Yu, J., Smith, D. L. & Smith, J. B. Thermal stability of human α-crystallins sensed by amide hydrogen exchange. *Protein Sci.* **13**, 332–341 (2004).
48. Jehle, S. et al. N-terminal domain of αB-crystallin provides a conformational switch for multimerization and structural heterogeneity. *Proc. Natl. Acad. Sci. USA* **108**, 6409–6414 (2011).
49. Mainz, A. et al. The chaperone αB-crystallin uses different interfaces to capture an amorphous and an amyloid client. *Nat. Struct. Mol. Biol.* **22**, 898–905 (2015).
50. Sluchanko, N. N. et al. Structural basis for the interaction of a human small heat shock protein with the 14–3–3 universal signaling regulator. *Structure* **25**, 305–316 (2017).
51. Pasta, Y., Raman, B., Ramakrishna, T. & Rao Ch. M. Role of the conserved SRLFDQFFG region of α-crystallin, a small heat shock protein. Effect on oligomeric size, subunit exchange, and chaperone-like activity. *J. Biol. Chem.* **278**, 51159–51166 (2003).
52. Baldwin, A. et al. Quaternary dynamics of αB-crystallin as a direct consequence of localised tertiary fluctuations in the C-terminus. *J. Mol. Biol.* **413**, 310–320 (2011).
53. Alderson, T. R., Benesch, J. L. P. & Baldwin, A. J. Proline isomerization in the C-terminal region of HSP27. *Cell Stress Chaperones* **22**, 639–651 (2017).
54. Jehle, S. et al. Solid-state NMR and SAXS studies provide a structural basis for the activation of αB-crystallin oligomers. *Nat. Struct. Mol. Biol.* **17**, 1037–1042 (2010).
55. Braun, N. et al. Multiple molecular architectures of the eye lens chaperone αB-crystallin elucidated by a triple hybrid approach. *Proc. Natl. Acad. Sci. USA* **108**, 20491–20496 (2011).
56. Pasta, S. Y., Raman, B., Ramakrishna, T. & Rao, C. M. The IXI/V motif in the C-terminal extension of α-crystallins: alternative interactions and oligomeric assemblies. *Mol. Vis.* **10**, 655–662 (2004).
57. Li, Y., Schmitz, K. R., Salerno, J. C. & Koretz, J. F. The role of the conserved COOH-terminal triad in αA-crystallin aggregation and functionality. *Mol. Vis.* **13**, 1758–1768 (2007).
58. Alderson, T. R. et al. Local unfolding of the HSP27 monomer regulates chaperone activity. *Nat. Commun.* https://doi.org/10.1038/s41467-019-08557-8 (2019).
59. Chen, J., Feige, M., Franzmann, T. M., Bepperling, A. & Buchner, J. Regions outside the α-crystallin domain of the small heat shock protein Hsp26 are required for its dimerization. *J. Mol. Biol.* **398**, 122–131 (2010).
60. Huber-Wunderlich, M. & Glockshuber, R. A single dipeptide sequence modulates the redox properties of a whole enzyme family. *Fold Des.* **3**, 161–171 (1998).

61. Bova, L. M., Sweeney, M. H., Jamie, J. F. & Truscott, R. J. W. (2001) Major changes in human ocular UV protection with age. *Invest. Ophthalmol. Vis. Sci.* **42**, 200–205 (2001).
62. Grey, A. C., Demarais, N. J., Brandi, J., West, B. J. & Donaldson, P. J. A quantitative map of glutathione in the aging human lens. *Int. J. Mass Spec.* https://doi: org/10.1016/j.ijms.2017.10.008 (2017).
63. Hogg, P. J. Disulfide bonds as switches for protein function. *Trends Biochem. Sci.* **28**, 210–214 (2003).
64. Lou, M. F. Redox regulation in the lens. *Prog. Ret. Eye Res.* **22**, 657–682 (2003).
65. Rost, J. & Rapoport, S. Reduction-potential of glutathione. *Nature* **201**, 185 (1964).
66. Simpson, R. J. Estimation of Free Thiols and Disulfide Bonds Using Ellman's Reagent. *Cold Spring Harb. Protoc. (*2008). doi: 10.1101/pdb.prot4699.
67. Stafford, W.F. III. Boundary analysis in sedimentation transport experiments: a procedure for obtaining sedimentation coefficient distributions using the time derivative of the concentration profile. *Anal. Biochem.* **203**, 295–301(1992).
68. Tang, G. et al. EMAN2: an extensible image processing suite for electron microscopy. *J. Struct. Biol.* **157**, 38–46 (2007).
69. van Heel, M., Harauz, G., Orlova, E. V., Schmidt, R. & Schatz, M. A new generation of the IMAGIC image processing system. *J. Struct. Biol.* **116**, 17–24 (1996).
70. Royer, C. A., Mann, C. J. & Matthews, C. R. Resolution of the fluorescence equilibrium unfolding profile of trp aporepressor using single tryptophan mutants. *Protein Sci.* **11**, 1844–1852 (1993).
71. Wei, H., Ahn, J., Yu, Y. Q., Tymiak, A., Engen, J. R., Chen, G. Using hydrogen/deuterium exchange mass spectrometry to study conformational changes in granulocyte colony stimulating factor upon PEGylation. *J Am Soc Mass Spectrom***. 23**, 498-504 (2012)
72. Korinek, A., Beck, F., Baumeister, W., Nickell, S. & Plitzko, J. M. Computer controlled cryo-electron microscopy - TOM^2 a software package for high-throughput applications. *J. Struct. Biol.* **175**, 394–405 (2011).
73. Heymann, J. B. & Belnap, D. M. (2007) Bsoft: Image processing and molecular modeling for electron microscopy. *J. Struct. Biol.* **157**, 3–18 (2007).
74. van Heel, M. Angular reconstitution: a posteriori assignment of projection directions for 3D reconstruction. *Ultramicroscopy* **21**, 111-123 (1987).
75. Rosenthal, P. B. & Henderson, R. Optimal determination of particle orientation, absolute hand, and contrast loss in single-particle electron cryomicroscopy. *J. Mol. Biol.* **333**, 721–745 (2003).
76. Lawson, C. L. et al. EMDataBank unified data resource for 3DEM. *Nucleic Acids Res.* **44**, D386–D403 (2016).

77. Goddard, T. D., Huang, C. C. & Ferrin, T. E. Visualizing density maps with UCSF Chimera. *J. Struct. Biol.* **157**, 281–287 (2007).
78. Penczek, P. A., Yang, C., Frank, J. & Spahn, C. M. Estimation of variance in single-particle reconstruction using the bootstrap technique. *J. Struct. Biol.* **154**, 168–183 (2006).
79. Vranken, W. F. et al. The CCPN data model for NMR spectroscopy: development of a software pipeline. *Proteins* **59**, 687–696 (2005).
80. Maiolica, A. et al. Structural analysis of multiprotein complexes by cross-linking, mass spectrometry, and database searching. *Mol. Cell. Proteomics* **6**, 2200–2211 (2007).
81. Rappsilber, J., Mann, M. & Ishihama, Y. Protocol for micro-purification, enrichment, pre-fractionation and storage of peptides for proteomics using StageTips. *Nat. Protoc.* **2**, 1896–1906 (2007).
82. Rappsilber, J., Ishihama, Y. & Mann, M. Stop and go extraction tips for matrix-assisted laser desorption/ionization, nanoelectrospray, and LC/MS sample pretreatment in proteomics. *Anal. Chem.* **75**, 663–670 (2003).
83. Cox, J., Mann, M. MaxQuant enables high peptide identification rates, individualized p.p.b.-range mass accuracies and proteome-wide protein quantification. *Nat. Biotechnol.* **26**, 1367–1372 (2008).
84. Mendes, M. L. et al. An integrated workflow for cross-linking/mass spectrometry. *bioRxiv* doi: https://doi.org/10.1101/355396 (2018).
85. Lenz, S., Giese, S. H., Fischer, L., & Rappsilber, J. In-search assignment of monoisotopic peaks improves the identification of cross-linked peptides. *J. Proteome Res.* **17***,* 3923–3931 (2018).
86. Fischer, L. & Rappsilber, J. Quirks of error estimation in cross-linking/mass spectrometry. *Anal. Chem.* **89**, 3829-3833 (2017).
87. Webb, B. & Sali, A. Comparative protein structure modeling using MODELLER. *Curr. Protoc. Bioinformatics* **47**, 1–32 (2014).
88. Roy, A., Kucukural, A. & Zhang, Y. I-TASSER: A unified platform for automated protein structure and function prediction. *Nat. Protoc.* **5**, 725–738 (2010).
89. Chacón, P. & Wriggers, W. Multi-resolution contour-based fitting of macromolecular structures. *J. Mol. Biol.* **317**, 375–384 (2002).
90. Case, D. A. et al. AMBER 16. University of California, San Francisco (2016).
91. Wu, X., Subramaniam, S., Case, D. A., Wu, K. W. & Brooks, B. R. Targeted conformational search with map-restrained self-guided Langevin dynamics: application to flexible fitting into electron microscopic density maps. *J. Struct. Biol.* **183**, 429–440 (2013).

92. Jorgensen, W. L., Chandrasekhar, J., Madura, J., Impey, R. W. and Klein, M. L. Comparison of simple potential functions for simulating liquid water. *J. Chem. Phys.* **79**, 926–935 (1983).

Figure legends

Figure 1: Cryo-EM 3D-reconstructions of human αA-crystallin (reduced) oligomers.
a) 12-mer (D3 symmetry) viewed along a 3-fold (left) (top view) and 2-fold symmetry axes (middle, right) (side views). The volume corresponding to an αA-crystallin dimer is indicated by a black ellipse. Apical (ap) and equatorial (eq) regions of the barrel-shaped 12-mer are marked by dashed ellipses.Top and side views of the 16-mer (D4 symmetry) (**b**) and of the 20-mer (D5 symmetry) (**c**). For clarity, three tetramers of the 16-mer are outlined. The empty arrowheads in **(a)** and **(b)** indicate the missing density between two adjacent tetramers in the equatorial plane of the barrel, the filled arrowhead in **(c)** the inter-tetramer density. Scale bar: 10 nm. The isosurface thresholds were set to render a volume corresponding to a protein mass of 239 kDa for the 12-mer, 318 kDa for the 16-mer, and 398 kDa for the 20-mer.

Figure 2: Pseudo-atomic models of human αA-crystallin (reduced) 16-mer.
a) Top and side views of the cryo-EM map of αA-crystallin 16-mer (reduced) superimposed with the atomic model (ribbon representation) containing the CTRs of apical (M_{ap}) and equatorial (M_{eq}) protomers in a non-3D domain-swapped conformation. ap-NI: apical N-terminal interface; eq-NI: equatorial N-terminal interface (black dashed ellipse). **b)** 16-mer containing the CTRs of M_{eq} in a 3D domain-swapped conformation. eq-CI: equatorial C-terminal interface (black solid ellipse). **c)** The domain organisation of human αA-crystallin. NTR (residues 1–60, sienna), ACD (residues 61–145, gray), CTR (residues 146-173, green). **d)** Close-up view of the eq-NI with intermolecular cross-links involving the residues M1 and K11. **e)** Close-up view of two neighboring equatorial protomers with their CTRs in non-3D domain-swapped configuration. The IPV motifs are shown in orange, β4- and β8-strands in light blue. **f)** Close-up view of eq-CI. Negatively and positively charged residues located within the CTRs are shown in red and blue, respectively.

Figure 3: CTR interactions in the reduced αA-crystallin oligomer ensemble.
a) αA_{red} 12-mer superimposed with the pseudo-atomic model containing the CTRs of both M_{ap} and M_{eq} in a non-3D domain-swapped conformation. **b)** αA_{red} 20-mer superimposed with the pseudo-atomic model containing the CTRs of M_{eq} in a 3D domain-swapped conformation. Domain color coding is as in Fig. 2. Dashed lines indicate the inter-protomer distances (measured as the distance between I146 and P160 of neighboring protomers) to be spanned by the linker between β9 and β10 for 3D domain-swap. **c)** ^{1}H, ^{15}N HSQC solution-state NMR spectrum of αA_{red}. In the inset, assigned backbone resonances involving the residues G149-S173 are shown in black, non-detectable residues in grey. **d)** Alignment of an equatorial, non-3D domain-swapped protomer ($M_{eq\text{-}nds}$, gray) with an equatorial, 3D domain swapped protomer

($M_{eq\text{-}ds}$, blue). The positions of C131, C142, G149 and of the IPV motif are indicated. **e)** PRE intensity ratios of a ^{15}N- and spin-labelled sample (^{15}N αA_{red}-IPSL) as a function of the residue number. As the spin label is attached to ^{15}N-labelled protein, intra- and intermolecular PREs are not distinguishable. **f)** PRE intensity ratios of a mixed sample containing ^{15}N-labelled αA_{red} (^{15}N-αA_{red}) and unlabeled protein bearing the spin label (^{14}N-αA_{red}-IPSL) in a 1:1 ratio (^{15}N-αA_{red}+^{14}N-αA_{red}-IPSL). As the spin label is attached to ^{14}N-αA, only intermolecular contacts lead to signal quenching.

Figure 4: Intramolecular disulfide cross-linking in human αA-crystallin.

a) Denaturing, non-reducing PAGE of αA_{red} incubated at 43 °C for 20 h in the presence of different GSH:GSSG ratios from fully oxidizing (2.5 mM GSSG) to fully reducing (5 mM GSH) conditions. ox: oxidized αA-crystallin; red: reduced αA-crystallin; 2-mer, 3-mer: disulfide-linked dimers and trimers. Note that even in the presence of 2.5 mM GSH minute amounts of intermolecular disulfide-bonded dimers form, likely as a result from GSSG-impurities present in the commercial GSSG-preparation. **b)** The same titration as in **(a)** using αA_{ox} at reaction start. **c)** Relative intensities of the αA_{red} and αA_{ox} monomer bands of the gels shown in **(a)** and **(b)** as a function of the GSH^2:GSSG ratio. Half-maximal oxidation (dashed line) at a redox potential of -135 mV (K_{eq}: 0.434 mM) for αA_{red} and at -145 mV (K_{eq}: 0.92 mM) for αA_{ox}. **d)** Denaturing, non-reducing PAGE of αA_{red} incubated for 20 h at 43 °C in the presence of 4.5 M urea and at varying GSH^2:GSSG ratios. Note that even under fully reducing conditions (5 mM GSH), approximately 50 % of αA-crystallin is oxidized, likely due to GSSG impurities. **e)** The same titration as in **(d)** using αA_{ox} at reaction start. **f)** Relative intensities of αA_{red} and αA_{ox} monomer bands of the gels shown in **(d)** and **(e)** as a function of the GSH^2:GSSG ratio. Half-maximal oxidation (dashed line) at a redox potential of – 222 mV (K_{eq}: 257 mM) for αA_{red} and -224 mV (K_{ox} 306 mM) for αA_{ox}. In **a-f**, the shaded area indicates the lenticular GSH^2:GSSG redox potential range.

Figure 5: Oligomer architecture of oxidized human αA-crystallin.

a) Electron micrographs of αA_{red} (left) and αA_{ox} (right) oligomers negatively stained with 2% uranyl acetate. Scale bar: 50 nm. Note the increased oligomer size and polydispersity in αA_{ox}. **b)** Size distributions of the oligomers of αA_{red} (black bars) and αA_{ox} (gray bars). The average oligomer size is shifted from ~13.5 nm in αA_{red} to ~17.7 nm in αA_{ox}. **c)** Different views of the 3D-reconstruction of a 32-meric assembly of αA_{ox}. Scale bar: 10 nm. Dimeric building blocks are indicated by ellipses.

Figure 6: Dynamics of oxidized human αA-crystallin

a) Relative fractional deuterium uptake (Rel frac D uptake) of all peptides detected in HDX-MS experiments. The deuteration behavior for early timepoints (10 s and 60 s) of the exchange-reaction is shown. Peptides ordered by their midpoint and the peptide start and end amino acid positions are indicated at the abscissa. Note that the uptake pattern is overall well conserved among αA_{red} and αA_{ox}. The error bars reflect the standard deviation, derived from triplicate determinations. **b)** Differences in amide hydrogen protection in αA_{red} and αA_{ox} mapped onto the model of a non-3D domain-swapped monomer of αA-crystallin. Differences in deuterium uptake were obtained by the difference in local relative deuterium uptake (ΔD uptake αA_{ox} - αA_{red}). The difference data were averaged using the algorithm DynamX 3.0 (Waters). Regions in αA_{ox} with unchanged protection from deuteration are colored white, with decreased protection red, and with increased protection blue.

Figure 7: αA-crystallin is capable of transferring disulfide bonds to human p53.

a) Heat-induced aggregation of recombinant p53 (2 µM) in the presence of a two-fold molar excess of GSSG, αA_{red}, αA_{ox} and reduced ($DsbA_{red}$) or oxidized ($DsbA_{ox}$) recombinant *E. coli* DsbA. Note that the aggregation of p53 is only suppressed in the presence of αA_{ox}. **b)** Non-reducing PAGE of samples withdrawn at the indicated timepoints (red arrows) from the aggregation assays in the presence of GSSG, αA_{ox} and $DsbA_{ox}$ shown in **(a)**. Note that disulfide-bridged species of p53 are formed both in the presence of αA_{ox} and $DsbA_{ox}$. **c)** Relative intensity of the p53 monomer band as a fraction of the intensity (amount of monomer) at the beginning of each aggregation kinetics experiment (t = 0 min).

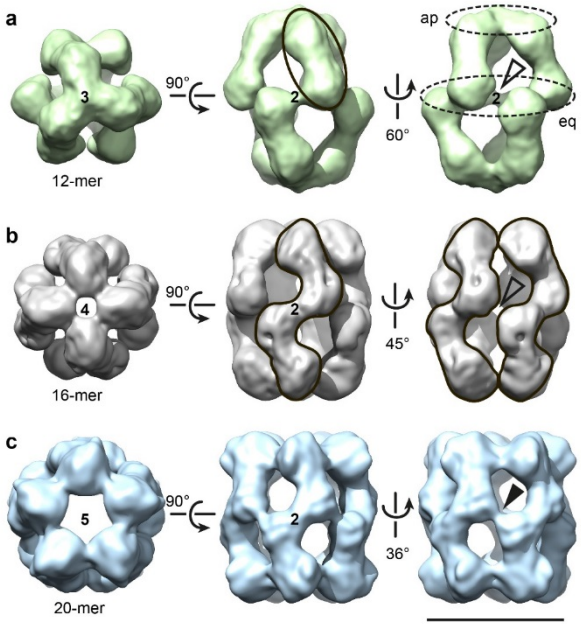

Figure 1

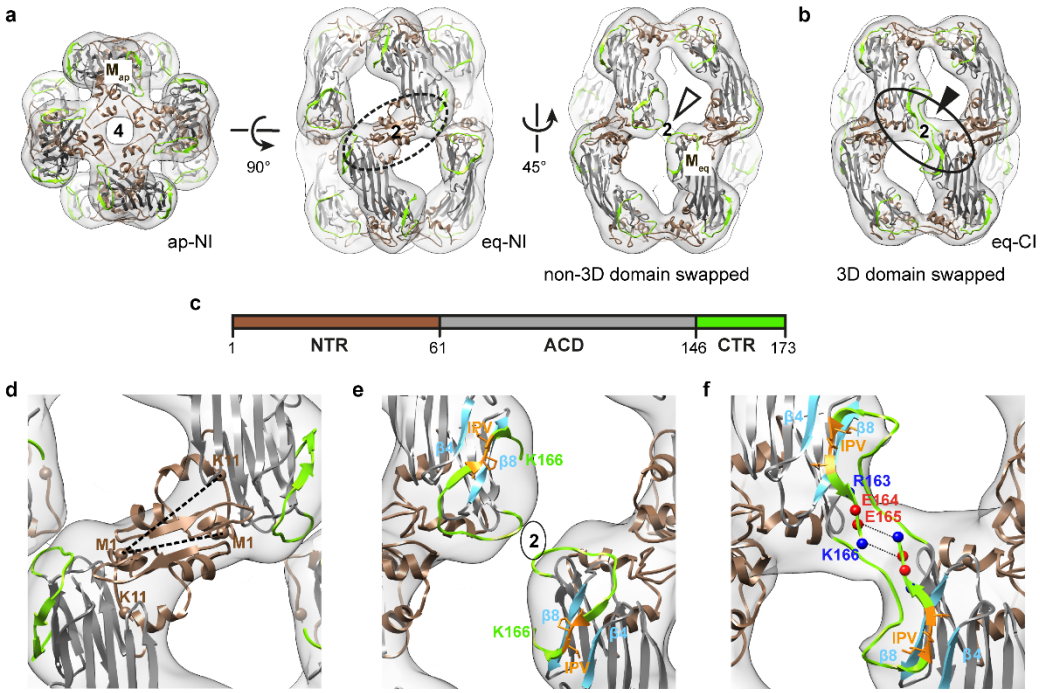
a
M_{ap}
4
ap-NI
90°
2
eq-NI
45°
2
M_{eq}
non-3D domain swapped
b
2
eq-CI
3D domain swapped
c
1
NTR
61
ACD
146
CTR
173
d
M1
M1
K11
e
IPV
β4
β8
K166
2
K166
β8
β4
IPV
f
β4
β8
IPV
R163
E164
E165
K166
IPV
β8
β4

Figure 2

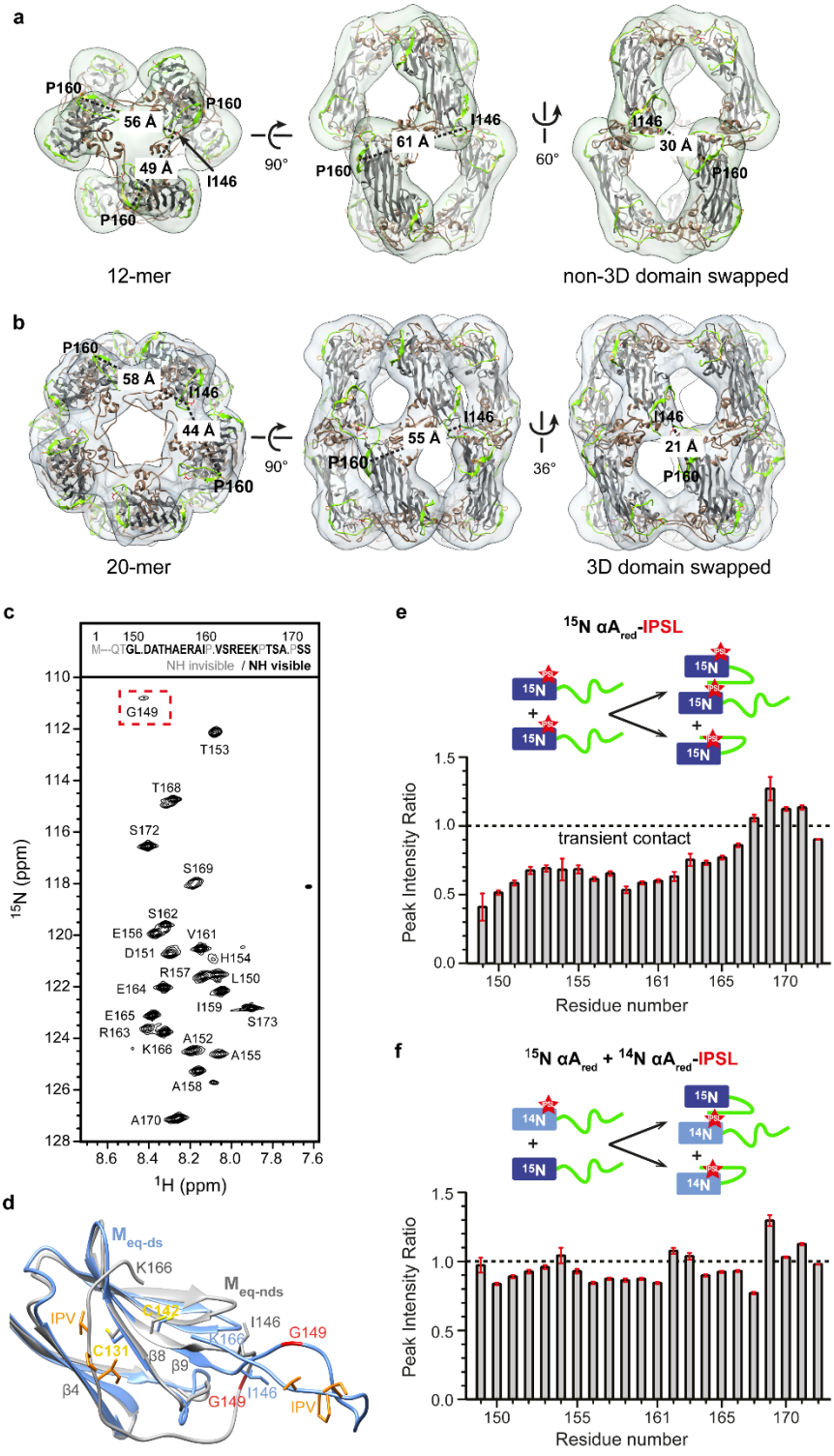
a
P160
56 Å
P160
49 Å
I146
P160
90°
61 Å
I146
P160
60°
I146
30 Å
P160
12-mer
non-3D domain swapped
b
P160
58 Å
I146
44 Å
P160
90°
55 Å
I146
P160
36°
I146
21 Å
P160
20-mer
3D domain swapped
c
1 150 160 170
M---QTGLDATHAERAIPVSREEKPTSAPSS
NH invisible / NH visible
15N (ppm)
1H (ppm)
G149
T153
T168
S172
S169
S162
E156
V161
D151
H154
R157
L150
E164
I159
S173
E165
R163
A152
K166
A155
A158
A170
d
Meq-ds
K166
Meq-nds
IPV
C142
I146
K166
G149
C131
β8
β9
β4
G149
I146
IPV
e
15N αAred-IPSL
15N
transient contact
Peak Intensity Ratio
Residue number
f
15N αAred + 14N αAred-IPSL
14N
15N
Peak Intensity Ratio
Residue number

Figure 3

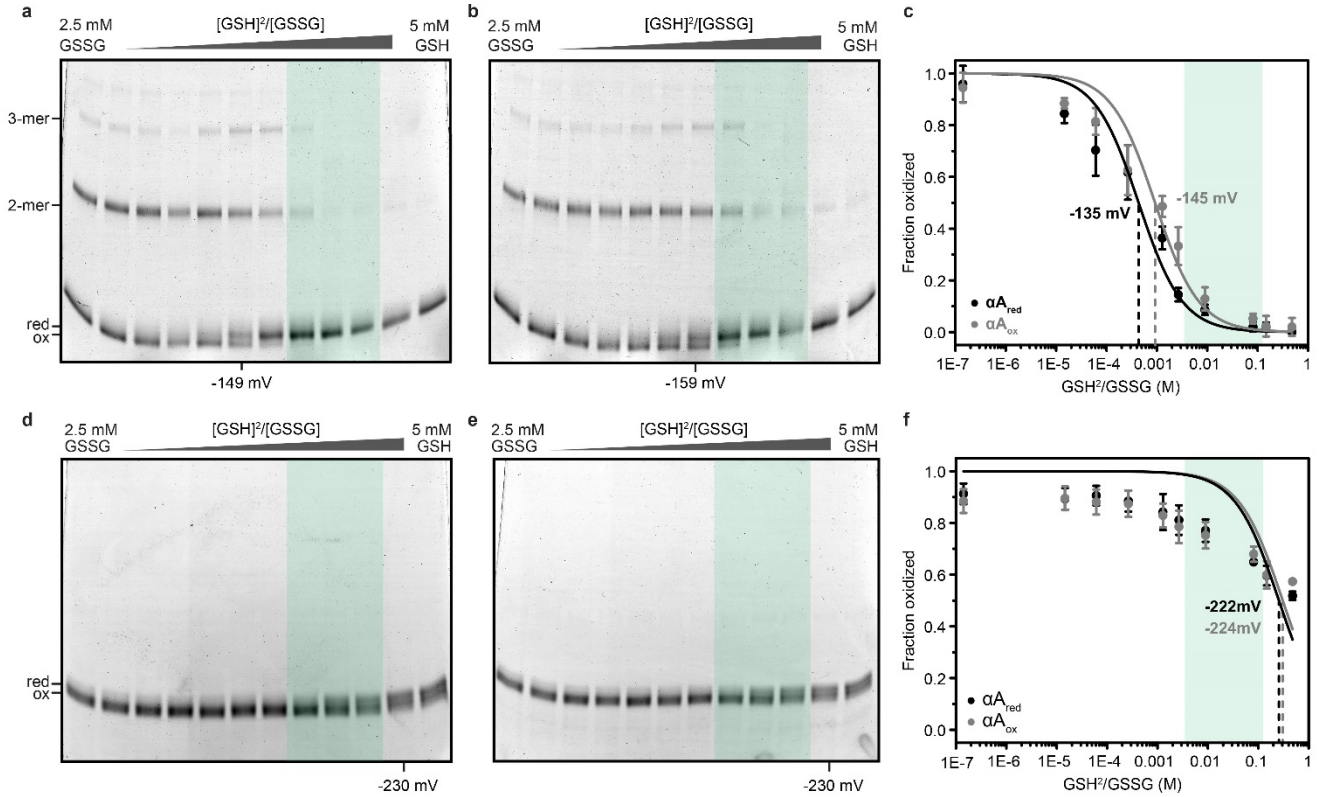
a
2.5 mM GSSG
[GSH]²/[GSSG]
5 mM GSH
3-mer
2-mer
red
ox
-149 mV
b
2.5 mM GSSG
[GSH]²/[GSSG]
5 mM GSH
-159 mV
c
Fraction oxidized
-135 mV
-145 mV
αA red
αA ox
GSH²/GSSG (M)
d
2.5 mM GSSG
[GSH]²/[GSSG]
5 mM GSH
red
ox
-230 mV
e
2.5 mM GSSG
[GSH]²/[GSSG]
5 mM GSH
-230 mV
f
Fraction oxidized
-222mV
-224mV
αA red
αA ox
GSH²/GSSG (M)

Figure 4

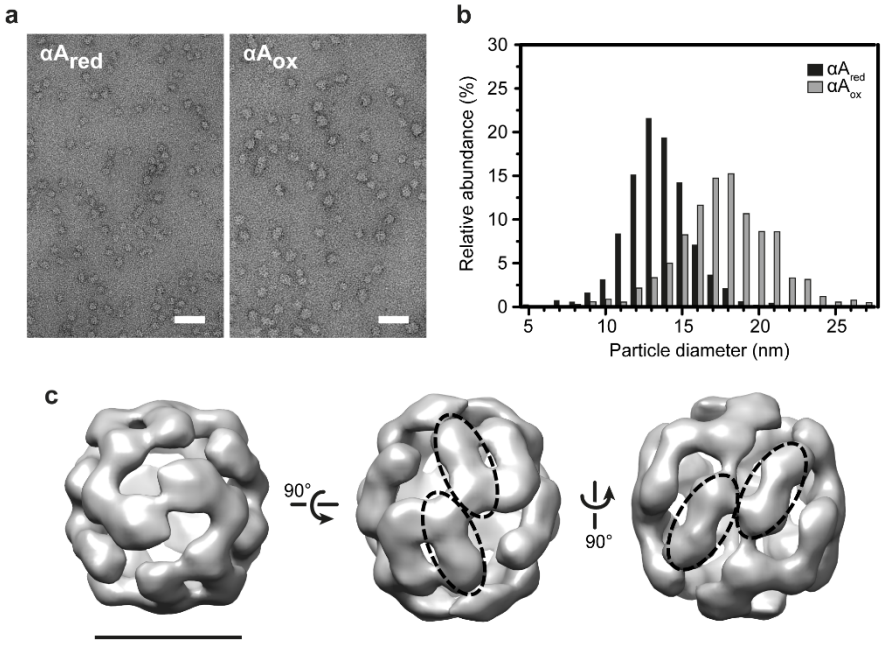
a
αA red
αA ox
b
Relative abundance (%)
Particle diameter (nm)
αA red
αA ox
c
90°
90°

Figure 5

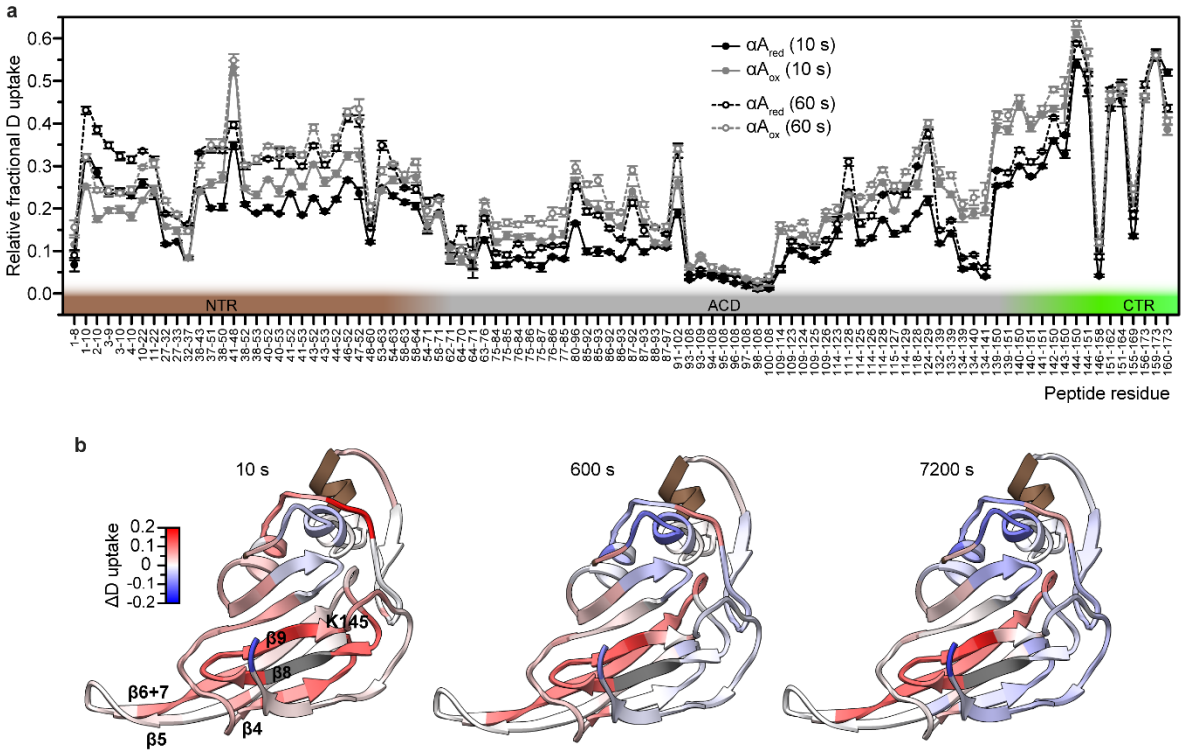
a
Relative fractional D uptake
αA_red (10 s)
αA_ox (10 s)
αA_red (60 s)
αA_ox (60 s)
NTR
ACD
CTR
Peptide residue
b
10 s
600 s
7200 s
ΔD uptake
0.2
0.1
0
-0.1
-0.2
K145
β9
β8
β6+7
β4
β5

Figure 6

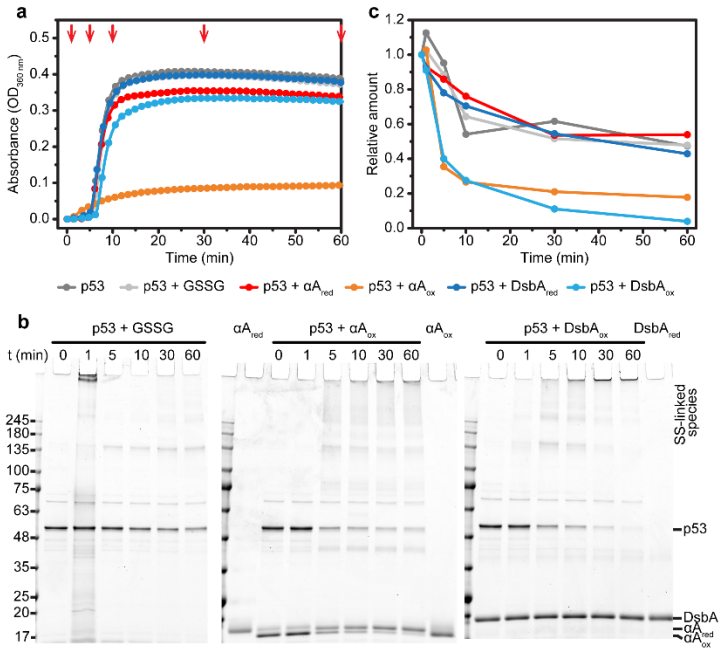
a
Absorbance (OD360 nm)
Time (min)
c
Relative amount
Time (min)
p53
p53 + GSSG
p53 + αAred
p53 + αAox
p53 + DsbAred
p53 + DsbAox
b
p53 + GSSG
αAred
p53 + αAox
αAox
p53 + DsbAox
DsbAred
t (min) 0 1 5 10 30 60
245
180
135
100
75
63
48
35
25
20
17
SS-linked species
p53
DsbA
αA
αAred
αAox

Figure 7